

Derivative-enhanced Deep Operator Network

Yuan Qiu^{*1}, Nolan Bridges^{†1}, and Peng Chen^{‡1}

¹College of Computing, Georgia Institute of Technology

Abstract

Deep operator networks (DeepONets), a class of neural operators that learn mappings between function spaces, have recently been developed as surrogate models for parametric partial differential equations (PDEs). In this work we propose a derivative-enhanced deep operator network (DE-DeepONet), which leverages the derivative information to enhance the prediction accuracy, and provide a more accurate approximation of the derivatives, especially when the training data are limited. DE-DeepONet incorporates dimension reduction of input into DeepONet and includes two types of derivative labels in the loss function for training, that is, the directional derivatives of the output function with respect to the input function and the gradient of the output function with respect to the physical domain variables. We test DE-DeepONet on three different equations with increasing complexity to demonstrate its effectiveness compared to the vanilla DeepONet.

Keywords: Neural operators, Operator learning, Derivative learning, DeepONet, dimension reduction, Adjoint method

1 Introduction

Using neural networks to approximate the maps between functions spaces governed by parametric PDEs can be very beneficial in solving many-query problems, typically arising from Bayesian inference, optimization under uncertainty, and Bayesian optimal experimental design. Indeed, once pre-trained on a dataset, neural networks are extremely fast to evaluate given unseen inputs, compared to traditional numerical methods like the finite element method. Recently many architectures are proposed to enhance the learning capacity, such as deep operator network (DeepONet) [11], physics-informed DeepONet [20], variational energy based DeepONet (V-DeepONet) [6], Fourier neural operator (FNO) [7], graph-based neural operator (GNO) [8], convolutional neural operator (CNO) [17]. Though these work demonstrate to be successful in approximating the output function, they do not necessarily provide accurate approximation of the derivative of the output with respect to the input, which typically needs to be computed many times in many problems in science and engineering such as PDE-constrained optimization problems for control, inference, and experimental design [13, 5].

*Email: yqiu327@gatech.edu

†Email: bridges@gatech.edu

‡Email: pchen402@gatech.edu

In this paper, we propose a novel method to enhance the performance of DeepONet through derivative-based dimension reduction and the incorporation of derivative information in the training. For the dimension reduction, we examine two projection bases: Karhunen–Loève Expansion (KLE) basis and active subspace method (ASM) basis. We incorporate derivative information by introducing additional losses, enabling the model to learn the operator more effectively when training data are limited.

Our work is related to the derivative-informed projected neural network (DIPNet) [16] and derivative-informed neural operator (DINO) [15] and presents an extension to enhance the performance of the DeepONet. The notable differences include: Unlike the encoder-decoder architecture employed in their work, we use the DeepONet architecture in constructing the neural network. Additionally, while the output in their papers are considered as the observations of the solution at a finite number of points, our approach can approximate the full solution field. Another difference is that we also incorporate the spatial derivatives in the training.

Our main contributions can be summarized as follows: (1) We propose a novel method that significantly improves DeepONet’s approximation accuracy for the output function, its directional derivative with respect to the input function, as well as its spatial derivatives, especially when the training samples are limited. (2) We provide the details on the computation of derivative labels of the solution of PDEs in a general form as well as the derivative-based dimension reduction to largely reduce the computational cost. (3) We demonstrate the effectiveness (enhanced approximation accuracy and computation cost) of our method through experiments conducted on three distinct PDEs with increasing complexities.

The rest of the paper is presented as follows: In Section 2 we present preliminaries of the problem setup, high fidelity approximation, and DeepONet, followed by Section 3 on the detailed presentation of DE-DeepONet and demonstration experiments in Section 4. Discussion of the conclusion and limitation is presented in the last section.

2 Preliminaries

This section presents the problem setup, high-fidelity approximation using finite element, and the vanilla DeepONet.

2.1 Problem Setup

Let $\Omega \subset \mathbb{R}^d$ denote an open and bounded domain with boundary $\partial\Omega \subset \mathbb{R}^{d-1}$, where the dimension $d = 1, 2, 3$. We consider a PDE of the general form defined in Ω as

$$\mathcal{R}(m, u) = 0, \tag{1}$$

prescribed with proper boundary conditions. Here $m \in V^{\text{in}}$ is an input parameter function defined in a separable Banach space V^{in} with probability measure ν and $u \in V^{\text{out}}$ is the output as the solution of the PDE defined in a separable Banach space V^{out} . Our goal is to construct a parametric model $\hat{u}(m; \theta)$ to approximate the solution operator that maps the parameter m to the solution u .

Once constructed, the parametric model $\hat{u}(m; \theta)$ should be much more computationally efficient to evaluate compared to solving the PDE with high fidelity approximation.

2.2 High Fidelity Approximation

For the high fidelity approximation of the solution, we consider using a *finite element method* [14] in this work. We partition the domain Ω into a finite set of subregions, called cells or elements. Collectively, these cells form a *mesh* of the domain Ω . Let h represent the diameter of the largest cell. We denote V_h^{in} indexed by h as the finite element space for the approximation of the input space V^{in} with Lagrange basis $\{\phi_1^{\text{in}}, \dots, \phi_{N_h^{\text{in}}}^{\text{in}}\}$ of dimension N_h^{in} such that $\phi_i^{\text{in}}(x^{(j)}) = \delta_{ij}$ at the finite element node $x^{(j)}$, with δ_{ij} being the Kronecker delta function. Similarly, we denote V_h^{out} as the finite element space for the approximation of the solution space V^{out} with basis $\{\phi_1^{\text{out}}, \dots, \phi_{N_h^{\text{out}}}^{\text{out}}\}$ of dimension N_h^{out} . Note that for the approximation to be high fidelity, N_h^{in} and N_h^{out} are often very large. To this end, we can write the high fidelity approximation of the input and output functions as

$$m_h(x) = \sum_{i=1}^{N_h^{\text{in}}} m_i \phi_i^{\text{in}}(x) \quad \text{and} \quad u_h(x) = \sum_{i=1}^{N_h^{\text{out}}} u_i \phi_i^{\text{out}}(x),$$

with coefficient vectors $\mathbf{m} = (m_1, \dots, m_{N_h^{\text{in}}})^T \in \mathbb{R}^{N_h^{\text{in}}}$ and $\mathbf{u} = (u_1, \dots, u_{N_h^{\text{out}}})^T \in \mathbb{R}^{N_h^{\text{out}}}$, whose entries are the *nodal values* of m and u at the corresponding nodes.

2.3 Vanilla DeepONet

We briefly review the DeepONet architecture [11] with a focus on learning the solution operator of the PDE (1). To predict the evaluation of solution function u at any point $x \in \Omega \cup \partial\Omega$ for any given input function m , [11] design a network architecture that comprises two separate neural networks: a trunk net $t(\cdot; \theta_t)$, which takes the coordinate values of the point x at which we want to evaluate the solution function as inputs, and a branch net $b(\cdot; \theta_b)$, which takes the vector \mathbf{m} encoding the parameter function m as inputs. In [11], the vector \mathbf{m} is the function evaluations at a finite set of fixed points $\{x^{(j)}\}_{j=1}^{N_h^{\text{in}}} \subseteq \Omega \cup \partial\Omega$, that is, $\mathbf{m} = (m(x^{(1)}), \dots, m(x^{(N_h^{\text{in}})}))^T$, which corresponds to coefficient vector in the finite element approximation with Lagrange basis at the same nodes. If the solution function is scalar-valued, then both neural networks output vectors of the same dimensions. The prediction is obtained by taking the standard inner product between these two vectors and (optionally) adding a real-valued bias parameter, i.e.,

$$\hat{u}(\mathbf{m}; \theta)(x) = \langle b(\mathbf{m}; \theta_b), t(x; \theta_t) \rangle + \theta_{\text{bias}},$$

with $\theta = (\theta_b, \theta_t, \theta_{\text{bias}})$. If the solution u is vector-valued of N_u components, i.e., $u = (u^{(1)}, \dots, u^{(N_u)})$, as in our experiments, we can use one of the four approaches in [12] to construct the DeepONet. Specifically, for each solution component, we use the same outputs of branch net with dimension N_b and different corresponding groups of outputs of trunk net to compute the inner product. More precisely, the solution $u^{(i)}$ of component $i = 1, \dots, N_u$, is approximated by

$$\hat{u}^{(i)}(\mathbf{m}; \theta)(x) = \langle b(\mathbf{m}; \theta_b), t^{(i)}(x; \theta_t) \rangle + \theta_{\text{bias}}^{(i)}, \quad (2)$$

where $t^{(i)}(x; \theta_t) = t(x; \theta_t)[(i-1)N_b + 1 : iN_b]$, the vector slice of $t(x; \theta_t)$ with indices ranging from $(i-1)N_b + 1$ to iN_b , $i = 1, \dots, N_u$.

For this construction, the outputs of the branch net can be interpreted as the coefficients of the basis learned through the trunk net. By partitioning the outputs of the trunk net into different

groups, we essentially partition the basis functions used for predicting different components of the solution. The DeepONet is trained using dataset $\mathcal{D} = \{(m^{(i)}, u^{(i)})\}_{i=1}^{N_{\mathcal{D}}}$ with $N_{\mathcal{D}}$ samples, where $m^{(i)}$ are random samples independently drawn from ν and $u^{(i)}$ are the solution of the PDE (with slight abuse of notation from the vector-valued solution) at $m^{(i)}$, $i = 1, \dots, N_{\mathcal{D}}$.

3 DE-DeepONet

The vanilla DeepONet uses the input parameter and output solution pairs as the labels for the model training. The approximation for the derivative of the solution with respect to the parameter (and the coordinate) are not necessarily accurate. However, in many downstream tasks such as Bayesian inference and experimental design, the derivatives are required. To better leverage our knowledge of the underlying PDE, we consider incorporating two additional derivative labels, that is, the Fréchet derivative $du(m; \cdot)$ and spatial derivative $\nabla_x u$, for the supervised training of the DeepONet, which we call derivative-enhanced DeepONet (DE-DeepONet). Let θ denote the trainable parameters in the DE-DeepONet. We propose to minimize the loss function

$$\begin{aligned} L(\theta) = & \lambda_1 \mathbb{E}_{m \sim \nu} \|u(m) - \hat{u}(m)\|_{L^2(\Omega)}^2 \\ & + \lambda_2 \mathbb{E}_{m \sim \nu} \|du(m; \cdot) - d\hat{u}(m; \cdot)\|_{\text{HS}}^2 \\ & + \lambda_3 \mathbb{E}_{m \sim \nu} \|\nabla_x u(m) - \nabla_x \hat{u}(m)\|_{L^2(\Omega)}^2, \end{aligned} \quad (3)$$

where the $L^2(\Omega)$ norm of a square integrable function f is defined as $\|f\|_{L^2(\Omega)}^2 = (\int_{\Omega} \|f(x)\|_2^2 dx)^{1/2}$, the Hilbert–Schmidt norm of an operator $T : H \rightarrow H$ that acts on a Hilbert space H is defined as $\|T\|_{\text{HS}}^2 = \sum_{i \in I} \|Te_i\|_H^2$, where $\{e_i\}_{i \in I}$ is an orthonormal basis of H . Here, $\lambda_i > 0, i = 1, 2, 3$ are hyperparameters that balance different loss terms.

The main challenge of minimizing the loss function (3) in practice is that with high fidelity approximation of the functions m and u using high dimensional vectors \mathbf{m} and \mathbf{u} , the term $\|du(m; \cdot) - d\hat{u}(m; \cdot)\|_{\text{HS}}^2$ (approximately) becomes $\|\nabla_{\mathbf{m}} \mathbf{u} - \nabla_{\mathbf{m}} \hat{\mathbf{u}}\|_F^2$, where the Frobenius norm of a matrix $M \in \mathbb{R}^{m \times n}$ is defined as $\|M\|_F^2 = \sum_{i=1}^m \sum_{j=1}^n M_{ij}^2$. It is a critical challenge to both compute and store the Jacobian matrix at each sample as well as to load and use it for training since it is often very large with size $N_h^{\text{out}} \times N_h^{\text{in}}$, with $N_h^{\text{in}}, N_h^{\text{out}} \gg 1$.

To tackle this challenge, we employ dimension reduction for the high dimensional input vector \mathbf{m} . The reduced representation of \mathbf{m} is given by projecting \mathbf{m} into a low dimensional linear space spanned by a basis $\boldsymbol{\psi}_1^{\text{in}}, \dots, \boldsymbol{\psi}_r^{\text{in}} \in \mathbb{R}^{N_h^{\text{in}}}$, with $r \ll N_h^{\text{in}}$, that is,

$$\tilde{\mathbf{m}} = (\langle \boldsymbol{\psi}_1^{\text{in}}, \mathbf{m} \rangle, \dots, \langle \boldsymbol{\psi}_r^{\text{in}}, \mathbf{m} \rangle)^T \in \mathbb{R}^r.$$

To better leverage the information of both the input probability measure ν and the map $u : m \rightarrow u(m)$, we consider the basis generated by active subspace method (ASM) using derivatives [21]. ASM identifies directions in the input space that significantly affect the output variance, or in which the output is most sensitive. See Section 3.3 for the detailed construction. In this case, the term $\mathbb{E}_{m \sim \nu} \|du(m; \cdot) - d\hat{u}(m; \cdot)\|_{\text{HS}}^2$ can be approximated by $\frac{1}{N_1 N_2} \sum_{i=1}^{N_1} \sum_{j=1}^{N_2} \|\nabla_{\tilde{\mathbf{m}}} u(m^{(i)})(x^{(j)}) - \nabla_{\tilde{\mathbf{m}}} \hat{u}(m^{(i)})(x^{(j)})\|_2^2$ with a small amount of functions $m^{(i)}$ sampled from input probability measure ν and points $x^{(j)}$ in the domain Ω . Note that $\nabla_{\tilde{\mathbf{m}}} \hat{u}(m^{(i)})(x^{(j)})$ is vector of size r , which is computationally feasible. For comparison, we also conduct experiments if the basis is the most commonly used Karhunen–Loève Expansion (KLE) basis.

We next formally introduces our DE-DeepONet, which uses dimension reduction for the input and incorporates two types of derivatives labels, that is, the directional derivative of output with respect to the input of the branch net and the derivative of output with respect to the input of the trunk net, as additional soft constraints into the loss function.

3.1 Model Architecture

We incorporate dimension reduction into DeepONet to construct a parametric model for approximating the solution operator. Specifically, if the solution is scalar-valued (the vector-valued case can be constructed similar to (2)), the prediction is given by

$$\hat{u}(\mathbf{m}; \theta)(x) = \langle b(\tilde{\mathbf{m}}; \theta_b), t(x; \theta_t) \rangle + \theta_{\text{bias}}, \quad (4)$$

where $\theta = (\theta_b, \theta_t, \theta_{\text{bias}})$ are the parameters to be learned. The branch net $b(\cdot; \theta_b)$ and trunk net $t(\cdot; \theta_t)$ can be chosen as MLP, ResNet, etc. Note that the branch net takes a small vector of the projected parameter as input.

3.2 Loss Function

In practical training of the DE-DeepONet, we formulate the loss function as follows

$$\begin{aligned} L(\theta) &= \frac{\lambda_1}{N_{\mathcal{D}}} \sum_{i=1}^{N_{\mathcal{D}}} \text{err}(\{\{\hat{u}(\mathbf{m}^{(i)}; \theta)(x^{(j)}), u(m^{(i)})(x^{(j)})\}\}_{j=1}^{N_x}) \\ &+ \frac{\lambda_2}{N_{\mathcal{D}}} \sum_{i=1}^{N_{\mathcal{D}}} \text{err}(\{\{\nabla_{\mathbf{m}} \hat{u}(\mathbf{m}^{(i)}; \theta)(x^{(j)}) \Psi^{\text{in}}, \Phi^{\text{out}}(x^{(j)}) (\nabla_{\mathbf{m}} \mathbf{u}(m^{(i)}) \Psi^{\text{in}}\}\}_{j=1}^{N_x}) \\ &+ \frac{\lambda_3}{N_{\mathcal{D}}} \sum_{i=1}^{N_{\mathcal{D}}} \text{err}(\{\{\nabla_x \hat{u}(\mathbf{m}^{(i)}; \theta)(x^{(j)}), \nabla_x u(m^{(i)})(x^{(j)})\}\}_{j=1}^{N_x}), \end{aligned} \quad (5)$$

where $\{x^{(j)}\}_{j=1}^{N_x}$ are the nodes of the mesh, $\Psi^{\text{in}} = (\boldsymbol{\psi}_1^{\text{in}} | \dots | \boldsymbol{\psi}_r^{\text{in}})$ is the matrix collecting the nodal values of the reduced basis of the input function space, and $\Phi^{\text{out}}(x) = (\phi_1^{\text{out}}(x), \dots, \phi_{N_h^{\text{out}}}^{\text{out}}(x))$ is the vector-valued function consisting of the finite element basis functions of the output function space. The $\text{err}(\{\{\mathbf{a}^{(i)}, \mathbf{b}^{(i)}\}\}_{i=1}^n)$ denotes the relative error between any two groups of vectors $\mathbf{a}^{(i)}$ and $\mathbf{b}^{(i)}$, computed as

$$\text{err}(\{\{\mathbf{a}^{(i)}, \mathbf{b}^{(i)}\}\}_{i=1}^n) = \frac{(\sum_{i=1}^n \|\mathbf{a}^{(i)} - \mathbf{b}^{(i)}\|_2^2)^{1/2}}{\varepsilon + (\sum_{i=1}^n \|\mathbf{b}^{(i)}\|_2^2)^{1/2}},$$

where $\varepsilon > 0$ is some small positive number to prevent the fraction dividing by zero.

In the following, we explain how to compute different loss terms in Equation (5)

- The first term is for matching the prediction of the parametric model $\hat{u}(\mathbf{m}^{(i)}; \theta)$ evaluated at any set of points $\{x^{(j)}\}_{j=1}^{N_x} \subseteq \Omega \cup \partial\Omega$ with the high fidelity solution $u(m^{(i)})$ evaluated at the same points. The prediction $\hat{u}(\mathbf{m}^{(i)}; \theta)(x^{(j)})$ is straightforward to compute using Equation (4). This involves passing the reduced branch inputs $\tilde{\mathbf{m}}^{(i)}$ and the coordinates of point $x^{(j)}$ into the branch net and trunk net, respectively. The label $u(m^{(i)})(x^{(j)})$ is obtained using finite element method solvers.

- The second term is for learning the directional derivative of the evaluation $u(x^{(j)})$ with respect to the input function m , in the direction of the reduced basis $\psi_1^{\text{in}}, \dots, \psi_r^{\text{in}}$. It can be shown that

$$\nabla_{\mathbf{m}} \hat{u}(\mathbf{m}^{(i)}; \theta)(x^{(j)}) \Psi^{\text{in}} = \nabla_{\tilde{\mathbf{m}}} \hat{u}(\mathbf{m}^{(i)}; \theta)(x^{(j)}).$$

Thus, the derivative of the outputs of the parametric model can be computed as the partial derivatives of the output with respect to the input of the branch net via automatic differentiation. On the other hand, the derivative labels

$$\Phi^{\text{out}}(x^{(j)}) (\nabla_{\mathbf{m}} \mathbf{u}(m^{(i)}) \Psi^{\text{in}}) = (du(m^{(i)}; \psi_1^{\text{in}})(x^{(j)}), \dots, du(m^{(i)}; \psi_r^{\text{in}})(x^{(j)}))$$

are obtained by first computing the Gateaux derivatives $du(m^{(i)}; \psi_1^{\text{in}}), \dots, du(m^{(i)}; \psi_r^{\text{in}})$ and then evaluating them at $x^{(j)}$. See Section 3.4 for details about the computation of the Gateaux derivative $du(m; \psi)$.

- The third term is for learning the spatial gradient of the output function u at point $x^{(j)}$. The gradient outputs $\nabla_x \hat{u}(\mathbf{m}^{(i)}; \theta)(x^{(j)})$ are also computed via automatic differentiation, with the partial derivative being taken with respect to the input of the trunk net. The gradient labels $\nabla_x u(m^{(i)})(x^{(j)})$ are computed using the gradient of the finite element basis.
- We initialize the loss weights $\lambda_i = 1$ for $i = 1, 2, 3$ and choose a loss balancing algorithm called the self-adaptive learning rate annealing algorithm [19] to update them at a certain frequency. This ensures that the gradient of each loss term have similar magnitudes, thereby enabling the neural network to learn all these labels simultaneously.

Remark. For the training, the computational cost of the second and third terms of the loss function (and their gradients) largely depends on the number of points used in each iteration. To reduce the computational and especially memory cost, we can use a subset of points, $N_x^{\text{batch}} = \alpha N_x$, where α is small number between 0 and 1 (e.g., $\alpha = 0.1$ or 0.15 in our experiments), in a batch of functions, though their locations could vary among different batches in one epoch. We find that this approach has little impact on the prediction accuracy of the model when N_x is large enough.

3.3 Dimension Reduction

Throughout the paper, we assume that the parameter functions m are independently drawn from some Gaussian random field [1]. In particular, we consider the case where the covariance function is the Whittle-Matern covariance function, that is, $m \stackrel{i.i.d.}{\sim} \mathcal{N}(\bar{m}, \mathcal{C})$, where \bar{m} is the (deterministic) mean function and $\mathcal{C} = (\delta I - \gamma \Delta)^{-2}$ (I is the identity and Δ is the Laplacian) is an operator such that the square root of its inverse, $\mathcal{C}^{-\frac{1}{2}}$, maps random function $(m - \bar{m})$ to Gaussian white noise with unit variance [9]. The parameters $\delta, \gamma \in \mathbb{R}^+$ jointly control the marginal variance and correlation length.

We consider two well-known linear projection bases for dimension reduction of the parameter function.

Karhunen–Loève Expansion (KLE) basis. The KLE basis is optimal in the sense that the mean-square error resulting from a finite representation of the random field m is minimized [4]. It

consists of eigenfunctions determined by the covariance function of the random field. Specifically, an eigenfunction ψ of the covariance operator $\mathcal{C} = (\delta I - \gamma \Delta)^{-2}$ satisfies the differential equation

$$\mathcal{C}\psi = \lambda\psi. \quad (6)$$

When solved using the finite element method, Equation (6) is equivalent to the following linear system (See Appendix A.1 for the derivation.)

$$M^{\text{in}}(A^{\text{in}})^{-1}M^{\text{in}}(A^{\text{in}})^{-1}M^{\text{in}}\boldsymbol{\psi} = \lambda M^{\text{in}}\boldsymbol{\psi}, \quad (7)$$

where the (i, j) -entries of matrices A^{in} and M^{in} are given by

$$A_{ij}^{\text{in}} = \delta\langle\phi_j^{\text{in}}, \phi_i^{\text{in}}\rangle + \gamma\langle\nabla\phi_j^{\text{in}}, \nabla\phi_i^{\text{in}}\rangle, \quad M_{ij}^{\text{in}} = \langle\phi_j^{\text{in}}, \phi_i^{\text{in}}\rangle.$$

Here, we recall that V_h^{in} is the finite element function space of input function, $\phi_i^{\text{in}}, i = 1, \dots, N_h^{\text{in}}$ for the finite element basis of V_h^{in} , and $\langle\cdot, \cdot\rangle$ for the $L^2(\Omega)$ -inner product. We select the first r (typically $r \ll N_h^{\text{in}}$) eigenfunctions $\psi_1^{\text{in}}, \dots, \psi_r^{\text{in}}$ corresponding to the r largest eigenvalues for the dimension reduction. Let $\Psi^{\text{in}} = (\boldsymbol{\psi}_1^{\text{in}} | \dots | \boldsymbol{\psi}_r^{\text{in}})$ denote the corresponding nodal values of these eigenfunctions. Since the eigenvectors $\boldsymbol{\psi}_i^{\text{in}}$ are M^{in} -orthogonal (or equivalently, eigenfunctions ψ_i^{in} are $L^2(\Omega)$ -orthogonal), the reduced representation of \boldsymbol{m} can be computed as $\widetilde{\boldsymbol{m}} = (\Psi^{\text{in}})^T M^{\text{in}}\boldsymbol{m}$, that is, the coefficients of the low rank approximation of \boldsymbol{m} in the linear subspace spanned by the eigenfunctions $\psi_1^{\text{in}}, \dots, \psi_r^{\text{in}}$.

Active Subspace Method (ASM) basis. The active subspace method is a gradient-based dimension reduction method that looks for directions in the input space contributing most significantly to the output variability [3]. In contrast to the KLE basis, the ASM basis is more computationally expensive. However, since the ASM basis captures sensitivity information in the input-output map rather than solely the variability of the input space, it typically achieves higher accuracy in predicting the output than KLE basis. We consider the case where the output is a multidimensional vector [21], representing the nodal values of the output function u . The ASM basis $\boldsymbol{\psi}$ satisfies the differential equation

$$\mathcal{H}\boldsymbol{\psi} = \lambda\mathcal{C}^{-1}\boldsymbol{\psi}, \quad (8)$$

where the action of operator \mathcal{H} on function $\boldsymbol{\psi}$ is given by

$$\mathcal{H}\boldsymbol{\psi} = \mathbb{E}_{m \sim \nu(m)}[d^*u(m; d\boldsymbol{\psi}(m))]. \quad (9)$$

Here, $du(m; \boldsymbol{\psi})$ is the Gateaux derivative of u at $m \in V_h^{\text{in}}$ in the direction of $\boldsymbol{\psi} \in V_h^{\text{in}}$, defined as $\lim_{\varepsilon \rightarrow 0}(u(m + \varepsilon\boldsymbol{\psi}) - u(m))/\varepsilon$, and $d^*u(m; \cdot)$ is the adjoint of the operator $du(m; \cdot)$. When solved using finite element method, Equation (8) is equivalent to the following linear system (See Appendix A.2 for the derivation.)

$$H\boldsymbol{\psi} = \lambda C^{-1}\boldsymbol{\psi}, \quad (10)$$

where the action of matrix H on vector $\boldsymbol{\psi}$ is given by

$$H\boldsymbol{\psi} = \mathbb{E}_{m \sim \nu(m)}[(\nabla_m \boldsymbol{u})^T M^{\text{out}}(\nabla_m \boldsymbol{u})\boldsymbol{\psi}], \quad (11)$$

and the action of matrix C^{-1} on vector $\boldsymbol{\psi}$ is given by

$$C^{-1}\boldsymbol{\psi} = A^{\text{in}}(M^{\text{in}})^{-1}A^{\text{in}}\boldsymbol{\psi}. \quad (12)$$

Here, M^{out} denotes the mass matrix of the output function space, i.e., $M_{ij}^{\text{out}} = \langle \phi_j^{\text{out}}, \phi_i^{\text{out}} \rangle$. In practice, when solving Equation (10), we obtain its left hand side through computing

$$\langle \langle \mathcal{H}\psi, \phi_1^{\text{in}} \rangle, \dots, \langle \mathcal{H}\psi, \phi_{N_h^{\text{in}}}^{\text{in}} \rangle \rangle^T$$

and its right hand side through the matrix-vector multiplication in Equation (12) (See Appendix A.2 for details). Similar to the KLE case, let Ψ^{in} denote the nodal values of r dominant eigenfunctions. Since the eigenvectors ψ_i^{in} are C^{-1} -orthogonal, the reduced representation of \mathbf{m} can be computed as $\widetilde{\mathbf{m}} = (\Psi^{\text{in}})^T C^{-1} \mathbf{m}$.

For the sake of scalability, we use the *double pass randomized algorithm* [18] in `hIPPYlib` (an open-source inverse problem python library) to solve the generalized eigenproblems Equation (7) and Equation (10).

3.4 Computation of the action of \mathcal{H}

By Equation (9), we use N_{grad} samples $\{(m^{(i)}, u^{(i)})\}_{i=1}^{N_{\text{grad}}}$ to compute the Monte Carlo estimate of the action of operator \mathcal{H} on any function $\psi \in V_h^{\text{in}}$, that is,

$$\mathcal{H}\psi \approx \frac{1}{N_{\text{grad}}} \sum_{i=1}^{N_{\text{grad}}} d^*u(m^{(i)}; du(m^{(i)}; \psi)). \quad (13)$$

Each summation term in Equation (13) can be obtained by computing $p := du(m; \psi)$ followed by $d^*u(m; p)$.

We first show how to compute p given the PDE residual $\mathcal{R}(m, u) = 0$. Since u is uniquely determined by m , we can write $u = u(m)$ so that $\mathcal{R}(m, u(m)) \equiv 0$ holds for any $m \in V_h^{\text{in}}$. Thus, for any $\varepsilon > 0$ and $\psi \in V_h^{\text{in}}$, we have

$$\mathcal{R}(m + \varepsilon\psi, u(m + \varepsilon\psi)) = 0.$$

Using the Taylor expansion we obtain

$$(\partial_m \mathcal{R}(m, u(m)))\varepsilon\psi + (\partial_u \mathcal{R}(m, u(m)))\delta u \approx 0, \quad (14)$$

where $\delta u = u(m + \varepsilon\psi) - u(m)$. Dividing both sides of Equation (14) by ε and letting ε approach 0 yields

$$(\partial_m \mathcal{R}(m, u(m)))\psi + (\partial_u \mathcal{R}(m, u(m)))du(m; \psi) = 0.$$

For ease of notation, we write

$$\partial_m \mathcal{R} = \partial_m \mathcal{R}(m, u(m)), \quad \partial_u \mathcal{R} = \partial_u \mathcal{R}(m, u(m)).$$

Then p is the solution to the linear PDE

$$(\partial_m \mathcal{R})\psi + (\partial_u \mathcal{R})p = 0. \quad (15)$$

We solve Equation (15) via its weak form

$$\langle (\partial_m \mathcal{R})\psi, v \rangle + \langle (\partial_u \mathcal{R})p, v \rangle = 0, \quad (16)$$

where v is a test function in V_h^{out} .

Next we show how to compute $d^*u(m; p)$. By Equation (15), we have $du(m; \psi) = -(\partial_u \mathcal{R})^{-1}(\partial_m \mathcal{R})\psi$. Thus,

$$\begin{aligned} w := d^*u(m; p) &= -(\partial_u \mathcal{R})^{-1}(\partial_m \mathcal{R})^*p \\ &= -(\partial_m \mathcal{R})^*(\partial_u \mathcal{R})^{-*}p. \end{aligned} \tag{17}$$

Let $q := (\partial_u \mathcal{R})^{-*}p$. We can solve for p via the weak form

$$\langle (\partial_u \mathcal{R})^*q, v \rangle = \langle p, v \rangle, \tag{18}$$

where v is a test function in V_h^{out} .

By Equation (17), we have $w = -(\partial_m \mathcal{R})^*q$. For any test function $v \in V_h^{\text{in}}$, it holds that

$$\begin{aligned} \langle w, v \rangle &= \langle -(\partial_m \mathcal{R})^*q, v \rangle \\ &= \langle q, -(\partial_m \mathcal{R})v \rangle. \end{aligned} \tag{19}$$

Note that we do not need to solve for w explicitly; we only compute $\langle w, v \rangle$ with v as the finite element basis functions $\phi_1^{\text{in}}, \dots, \phi_{N_h^{\text{in}}}^{\text{in}}$. The cost of computing the right hand side of Equation (19) arises from evaluating the directional derivative and its inner product with the finite element basis functions.

Remark. *When using the double pass randomized algorithm to obtain the first r eigenpairs in Equation (10), we need to compute the action of \mathcal{H} on $2(r+s)$ random functions in V_h^{in} (e.g., their nodal values are sampled from the standard Gaussian distribution), where $s \in \mathbb{N}^+$ is typically a small oversampling parameter, often chosen between 5 and 20. To speed up the computation, we first compute the LU factorization of the matrices resulting from the discretization of the linear PDEs in Equation (16) and Equation (18). Then the action of $d^*u(m^{(i)}; du(m^{(i)}; \cdot))$ on these random functions can be efficiently computed via the forward and backward substitution. Furthermore, the computational time can be significantly reduced by parallelizing the computation of the average value in Equation (13) across multiple processors.*

4 Experiments

In this section, we present experiment results to demonstrate the derivative-enhanced accuracy and cost of our method on three test PDEs, including both linear and nonlinear, both scalar-valued and vector-valued solutions. Details about the data generation and training can be found in Appendix B.

4.1 Input Probability Measure

In all test cases, we assume that the input functions $m^{(i)}$ are i.i.d. samples drawn from a Gaussian random field with mean function \bar{m} and covariance operator $(\delta I - \gamma \Delta)^{-\alpha}$, with $\alpha = 2$ so the covariance operator is of trace class. It is worth noting that the parameters γ and δ jointly control the marginal variance and correlation length, for which we take values to have large variation of the samples so that it is difficult for the neural network approximation with relatively large errors. We use a scalable sampling algorithm in [hippylib](#) [18] to generate the samples.

4.2 Governing Equations

We consider a linear and scalar-valued Darcy flow equation, a nonlinear vector-valued hyperelasticity equation with one state (displacement), and a nonlinear vector-valued Navier–Stokes equations with multiple states (velocity and pressure). Specifically, we learn the map from (the logarithm of) the diffusion coefficient field to the solution of the Darcy flow equation with zero Dirichlet boundary condition. For the hyperelasticity equation, we consider an experimental scenario where a square of hyperelasticity material is secured along its left edge while a fixed upward-right force is applied to its right edge [2]. Our goal is to learn the map between (the logarithm of) the material’s Young’s modulus and its displacement. Lastly, we consider the Navier–Stokes equations that describes viscous, incompressible fluid flow. In particular, we consider the lid-driven cavity case where a square cavity consisting of three rigid walls with no-slip conditions and a lid moving with a tangential unit velocity. We consider that the uncertainty comes from the viscosity term and aim to predict the velocity field.

Darcy flow equation. The strong form of the PDE can be written as

$$\begin{cases} -\nabla \cdot (e^m \nabla u) = 1, & x \in \Omega, \\ u(x) = 0, & x \in \partial\Omega. \end{cases}$$

Here, we assume that the randomness arises from the viscosity term e^m . For demonstration, we choose $\bar{m} = 0$, $\delta = 1.0$ and $\gamma = 0.1$. Note that the PDE is linear but the solution operator is not. See Figure 1 for the visualization for input-output pairs of the Darcy flow equation.

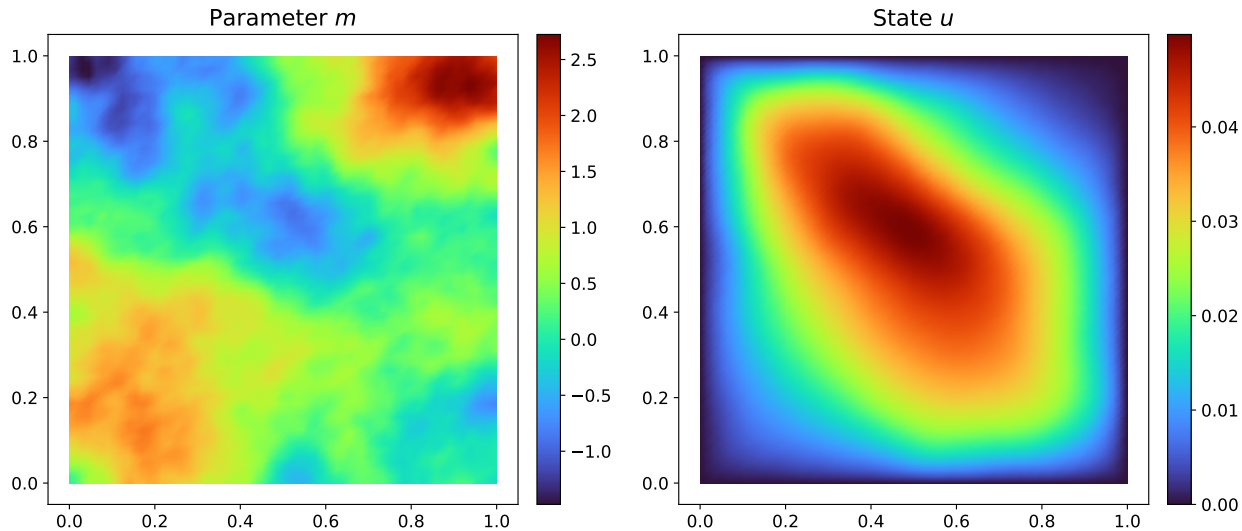


Figure 1: Visualization of input-output pairs of Darcy flow equation.

Hyperelasticity equation. We follow the problem setup in [2]. Write X (instead of x) for a material point in the domain Ω and $u = u(X) : \mathbb{R}^2 \rightarrow \mathbb{R}^2$ for the displacement of the material point. Under the influence of internal and/or external forces, the material point is mapped to a

spatial point $x = x(X) = X + u(X) : \mathbb{R}^2 \rightarrow \mathbb{R}^2$. Let $F = \nabla_X x = I + \nabla_X u : \mathbb{R}^2 \rightarrow \mathbb{R}^{2 \times 2}$ denote the deformation gradient. For a hyperelasticity material, the internal forces can be derived from a strain energy density

$$W(X, C) = \frac{\mu(X)}{2}(\text{tr}(C) - 3) + \frac{\lambda(X)}{2}(\ln(J))^2 - \mu(X) \ln(J).$$

Here, $C = F^T F$ is the right Cauchy-Green strain tensor, $\text{tr}(C)$ is the trace of matrix C , J is the determinant of matrix F , and $\mu(X), \lambda(X) : \mathbb{R}^2 \rightarrow \mathbb{R}$ are the Lamé parameters which we assume to be related to Young's modulus of elasticity $E(X) : \mathbb{R}^2 \rightarrow \mathbb{R}$ and Poisson ratio $\nu \in \mathbb{R}$

$$\mu(X) = \frac{E(X)}{2(1 + \nu)}, \quad \lambda(X) = \frac{\nu E(X)}{(1 + \nu)(1 - 2\nu)}.$$

We assume the randomness comes from the Young's modulus $E(X) = e^{m(X)} + 1$. Let $S = 2 \frac{\partial W}{\partial C}$ denote the second Piola-Kirchhoff stress tensor. We consider the case where the left boundary of the material is fixed, and the right boundary is subjected to stretching by an external force $t = t(X) : \mathbb{R}^2 \rightarrow \mathbb{R}^2$. The strong form of the steady state PDE can be written as

$$\begin{cases} \nabla_X \cdot (FS) = 0, & X \in \Omega, \\ u = 0, & X \in \Gamma_{\text{left}}, \\ FS \cdot n = 0, & X \in \Gamma_{\text{top}} \cup \Gamma_{\text{bottom}}, \\ FS \cdot n = t, & X \in \Gamma_{\text{right}}, \end{cases}$$

where $\Gamma_{\text{left}}, \Gamma_{\text{right}}, \Gamma_{\text{top}}$ and Γ_{bottom} denote the left, right, top, and bottom boundary of the material domain Ω , respectively, and n is the unit outward normal vector on the boundary. Our goal is to learn the operator that maps the parameter m to the displacement u . For demonstration, we choose $\bar{m} = 0$, $\delta = 0.4$, $\gamma = 0.04$, Poisson ratio $\nu = 0.4$, and the external force

$$t(X) = (0.06 \exp(-0.25|X_2 - 0.5|^2), 0.03(1 + 0.1X_2))^T.$$

In practice, we solve the PDE by first formulating the energy \widetilde{W} in the weak form

$$\widetilde{W} = \int_{\Omega} W dX - \int_{\Gamma_{\text{right}}} \langle t, u \rangle ds$$

and then solving for u that satisfies the stationary condition, that is, the equation

$$d\widetilde{W}(u; v) = 0,$$

holds for any test function v in the state space. See Figure 2 for the visualization for input-output pairs of the hyperelasticity equation.

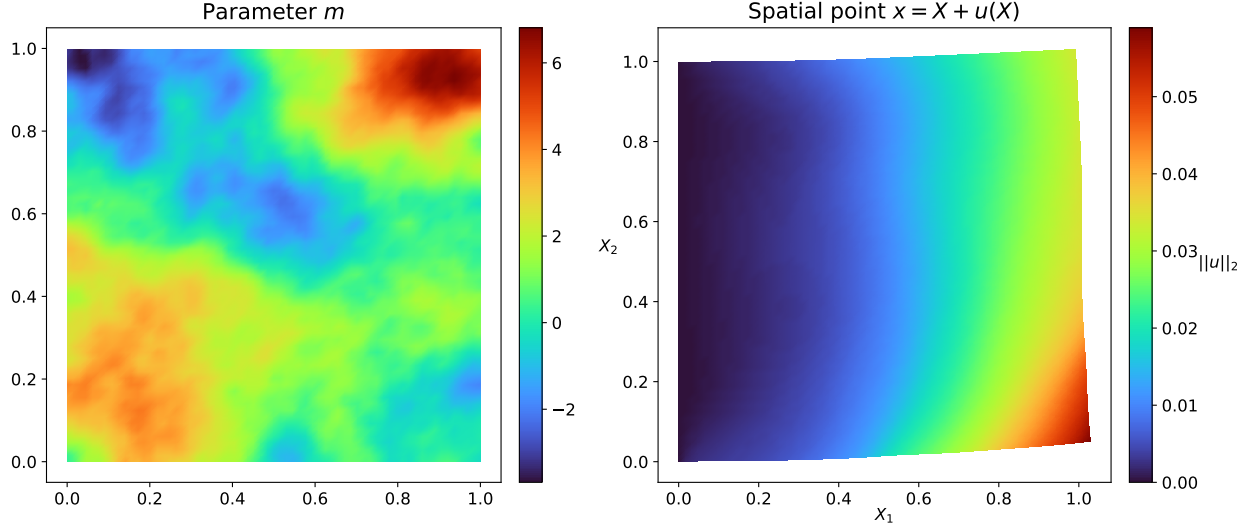


Figure 2: Visualization of input-output pairs of hyperelasticity equation.

Navier–Stokes equation. Let $u = u(x) \in \mathbb{R}^2$ and $p = p(x) \in \mathbb{R}$ denote the velocity and pressure at point $x \in \Omega = (0, 1)^2$. The strong form of the PDE can be written as

$$\begin{cases} -\nabla \cdot e^m \nabla u + (u \cdot \nabla)u + \nabla p = 0, & x \in \Omega, \\ \nabla \cdot u = 0, & x \in \Omega, \\ u = (1, 0)^T, & x \in \Gamma_{\text{top}}, \\ u = (0, 0)^T, & x \in \Gamma \setminus \Gamma_{\text{top}}, \end{cases}$$

where Γ_{top} and Γ denote the left and whole boundary of the cavity domain Ω , respectively. Here, we assume that the randomness arises from the viscosity term e^m . Our goal is learn the operator that maps the parameter m to the velocity u . For demonstration, we choose $\bar{m} = 6.908$ ($e^{\bar{m}} \approx 10^3$), $\delta = 0.6$, and $\gamma = 0.06$. See Figure 3 for the visualization for input-output pairs of the Navier–Stokes equations.

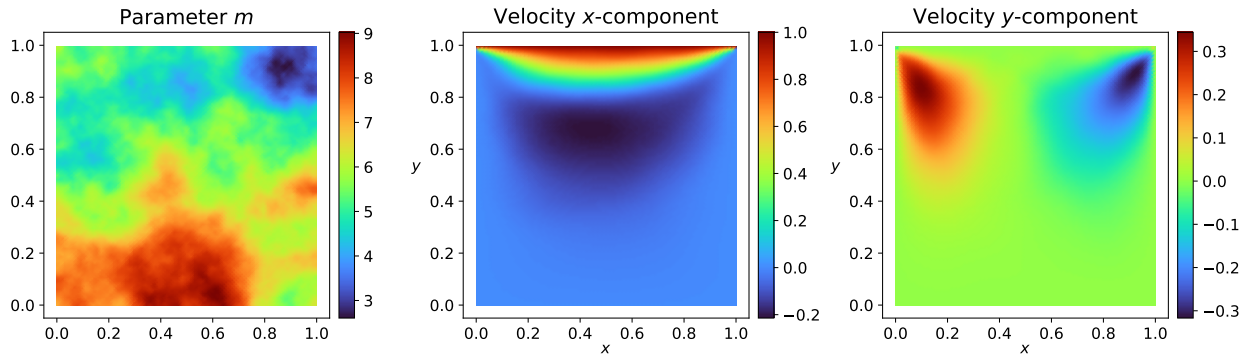


Figure 3: Visualization of input-output pairs of Navier–Stokes equations.

4.3 Evaluation Metrics

We use the following three metrics to evaluate the performance of different methods. For $u(m)(x)$ approximations, we compute the relative error in the $L^2(\Omega)$ norm and $H^1(\Omega)$ norm on the test dataset $\mathcal{D}_{\text{test}} = \{(m^{(i)}, u^{(i)})\}_{i=1}^{N_{\text{test}}}$, that is,

$$\frac{1}{N_{\text{test}}} \sum_{m^{(i)} \in \mathcal{D}_{\text{test}}} \frac{\|\hat{u}(m^{(i)}; \theta) - u(m^{(i)})\|_{L^2(\Omega)}}{\|u(m^{(i)})\|_{L^2(\Omega)}}, \quad \frac{1}{N_{\text{test}}} \sum_{m^{(i)} \in \mathcal{D}_{\text{test}}} \frac{\|\hat{u}(m^{(i)}; \theta) - u(m^{(i)})\|_{H^1(\Omega)}}{\|u(m^{(i)})\|_{H^1(\Omega)}},$$

where

$$\|u\|_{L^2(\Omega)} = \int_{\Omega} \|u(x)\|_2^2 dx = \mathbf{u}^T M^{\text{out}} \mathbf{u}, \quad \|u\|_{H^1(\Omega)} = (\|u\|_{L^2(\Omega)}^2 + \|\nabla u\|_{L^2(\Omega)}^2)^{1/2}.$$

For $du(m; \cdot)(x)$ approximations, we compute the relative error in the Frobenius norm on $\mathcal{D}_{\text{test}}$ along random directions $\omega = \{\omega_i\}_{i=1}^{N_{\text{dir}}}$, that is,

$$\frac{1}{|\mathcal{D}_{\text{test}}|} \sum_{m^{(i)} \in \mathcal{D}_{\text{test}}} \frac{\|d\hat{u}(m^{(i)}; \omega)(x) - du(m^{(i)}; \omega)(x)\|_F}{\|du(m^{(i)}; \omega)(x)\|_F},$$

where ω_i are samples drawn from the same distribution as m .

4.4 Main Results

We observe consistent performance in terms of enhanced approximation accuracy for the three different equations. Here we only present a part of the results for the Navier–Stokes equations and leave all other results for other equations, including also hyperparameter tuning in the training of the neural networks, the architecture of different neural networks, the configuration of data generations, the full set of test errors, visualization of the KLE and ASM basis functions, and visualization of the prediction of both the solution and derivatives in Appendix B. We show the tradeoff in terms of prediction error and computational cost of different methods. We find that the advantages of our method are especially evident for the more complex and challenging Navier–Stokes equations.

Test errors. In Figure 4, we show a comparison of different methods for predicting the velocity field in the y direction and its derivative with respect to parameter in the direction of $\{\omega_i\}_{i=1}^{N_{\text{dir}}}$ with $N_{\text{dir}} = 128$. We observe that the reduced basis DeepONet, even without using derivative labels for training, has a prediction error comparable to that of the vanilla DeepONet. This suggests that the chosen number of reduced bases ($r = 16$) is sufficiently large to predict a high-quality output function.

We also find that incorporating two additional derivative losses (denoted as ‘dm’ loss and ‘dx’ loss) into the training of the reduced basis DeepONet significantly lower the errors (to between one-thirds and one-half of their original values in predicting the velocity field in the y direction) in predicting both the solution u and its directional derivative with respect to the input function m . See Figure 5 and Figure 6 for a visualization comparing the prediction of velocity- y and its directional derivative, where the DE-DeepONet with ASM+dm+dx using the two derivative labels provides a more accurate prediction.

In addition, we conduct experiments for comparing the results of adding solely the ‘dm’ loss versus adding both ‘dm’ and ‘dx’ losses. The details are provided in Appendix B.3. We observe that incorporating ‘dm’ loss makes a dominant contribution to error reduction, while incorporating ‘dx’ loss has a relatively smaller effect on reducing the errors.

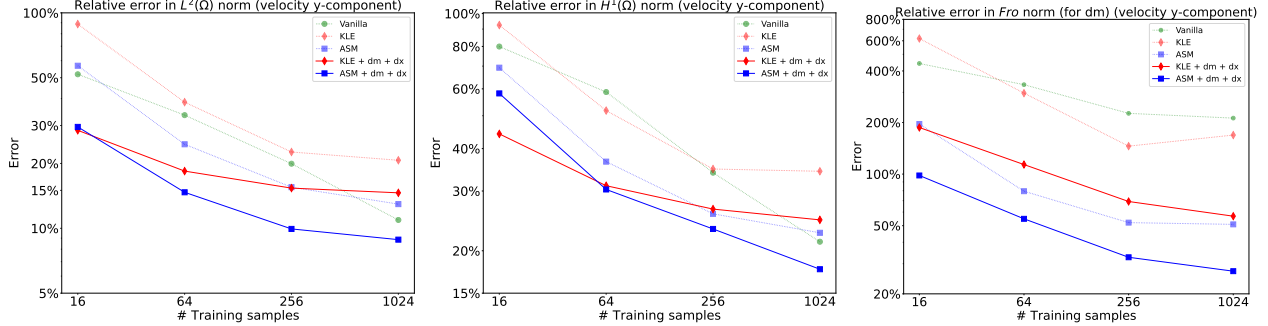


Figure 4: Mean relative errors over 5 trials with a varying number of training samples for the Navier–Stokes equations using different methods. Relative errors in the $L^2(\Omega)$ norm (left) and $H^1(\Omega)$ norm (middle) for the prediction of the velocity-y. Right: Relative error in the Frobenius (Fro) norm for the prediction of the derivative of the velocity-y with respect to the parameter in the direction of the 128 samples drawn from the same distribution as parameter.

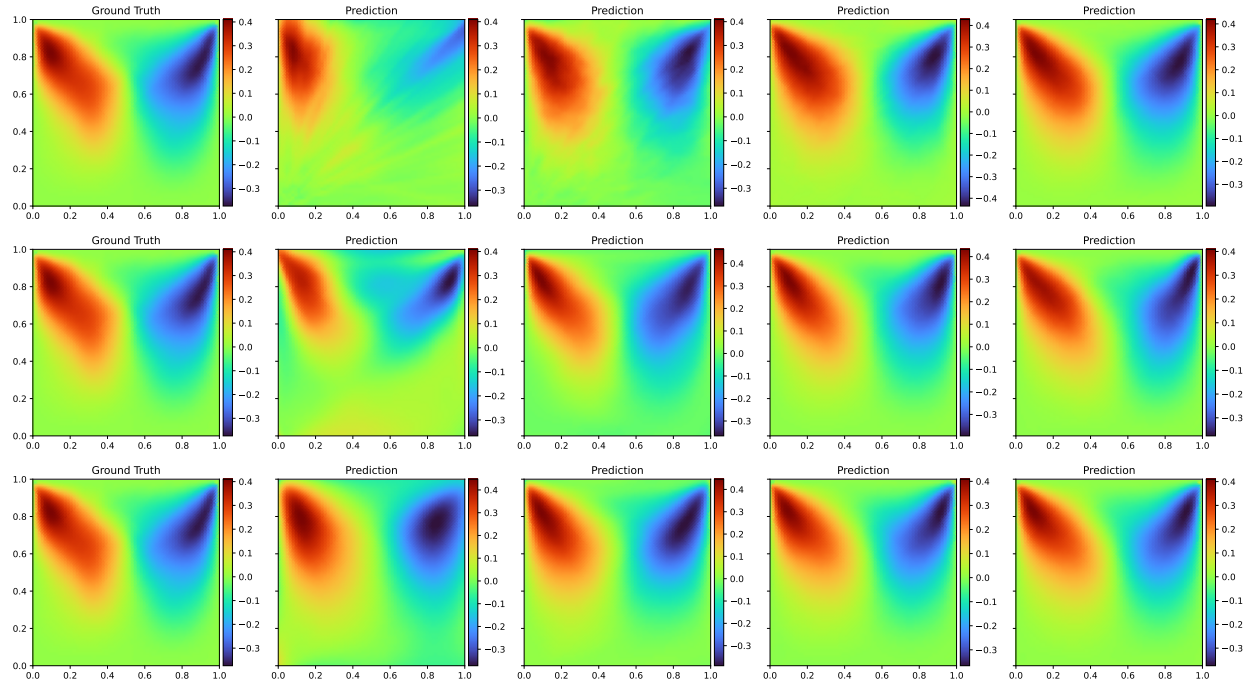


Figure 5: Comparison of the predictions of velocity-y with (16, 64, 256, 1024) training samples using different methods. Top: Vanilla DeepONet; Middle: ASM; Bottom: DE-DeepONet using ASM + dm + dx.

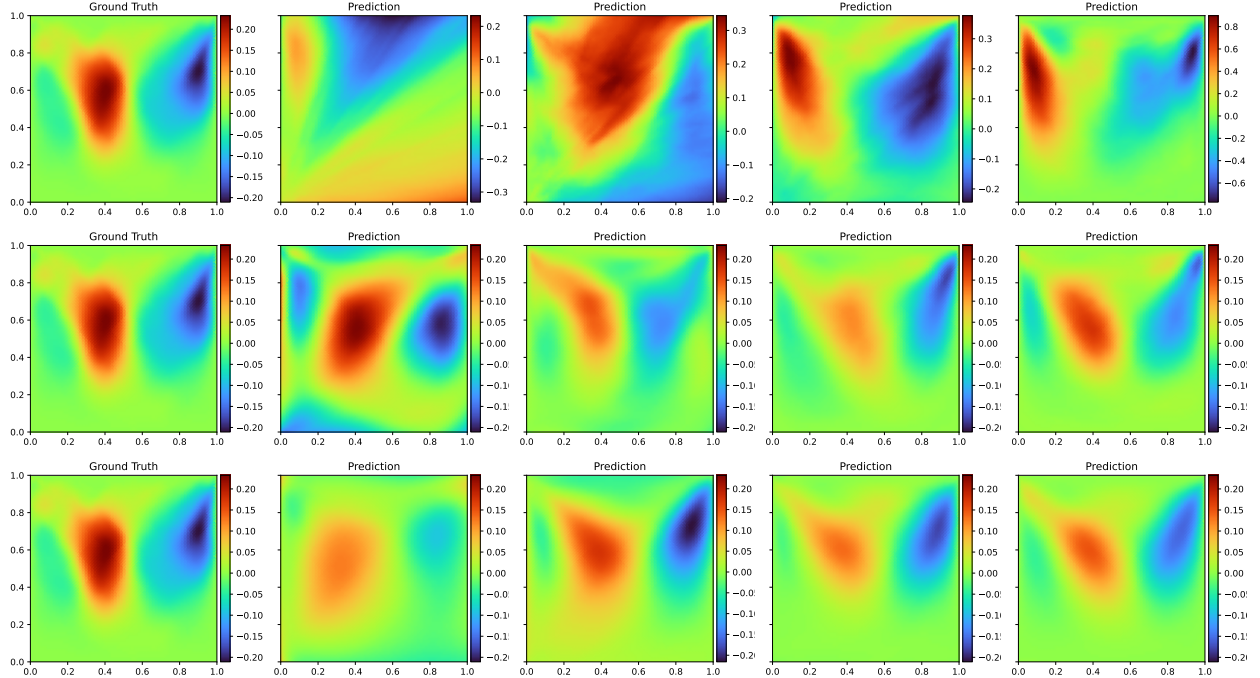


Figure 6: Comparison of the predictions of directional derivative $du_2(m; \omega_1)$ with (16, 64, 256, 1024) training samples using different methods. Top: Vanilla DeepONet; Middle: ASM; Bottom: DE-DeepONet using ASM + dm + dx.

Computational cost. We use MPI and the finite element library FEniCS [10] to distribute the computational load of offline data generation to 64 CPUs for all the PDEs considered in this work. See Table 1 for the wall clock time for generating the samples as Gaussian random fields (GRFs), solving the PDEs, computing the $r = 16$ reduced basis functions (KLE or ASM) corresponding to the 16 largest eigenvalues, generating the derivative labels dm and dx with respect to the parameter and space, respectively. Note that generating the derivative labels is more expensive than generating the PDE solutions, but not by large, especially for the more complex and expensive Navier–Stokes equations.

Table 1: Wall clock time (in seconds) for the data generation on 2 X AMD EPYC 7543 32-Core Processors

Dataset	Process					
	GRFs ($N_{\text{all}} = 2000$) (64 CPUs)	PDEs ($N_{\text{all}} = 2000$) (64 CPUs)	KLE ($r = 16$) (1 CPU)	ASM ($r = 16$) (16 CPUs)	dm labels ($N_{\text{all}} = 2000, r = 16$) (64 CPUs)	dx labels ($N_{\text{all}} = 2000$) (64 CPUs)
Darcy flow	1.1	1.4	0.4	1.1	8.3	4.6
Hyperelasticity	1.1	9.7	0.4	1.4	19.5	8.8
Navier–Stokes	1.9	99.1	1.3	9.7	125.5	45.8

We present comparisons of the computational cost of model training using different methods with two different number of training samples ($N_{\text{train}} = 64$, corresponding to a limited training dataset setting, and $N_{\text{train}} = 1024$, corresponding to a sufficient training dataset setting) in Table 2. We find that incorporating derivative losses leads to larger computational cost as expected. However, when the training data are limited, the increased computation cost is compensated for a significant reduction of errors. We note that there are potential ways to reduce the cost, e.g., by training the model with additional derivative losses only during the later stage of training, or by using fewer points for computing the derivative losses in each iteration. Additionally, the number of trainable parameters in the neural network is shown in Table 3. We observe that the reduced basis DeepONet has an order of magnitude fewer parameters than the vanilla DeepONet. Thanks to the dimension reduction in the input parameter, we are able to efficiently compute and store the derivatives as well as train the reduced basis DeepONet.

Table 2: Wall clock time (in seconds per epoch) for the neural network training on a single NVIDIA RTX A6000 GPU

Dataset	Method ($N_{\text{train}} = 64, N_{\text{train}} = 1024$)			
	Vanilla	Reduced	Reduced + dm	Reduced + dm + dx
Darcy flow	(0.04, 0.64)	(0.03, 0.50)	(0.09, 1.58)	(0.14, 2.39)
Hyperelasticity	(0.04, 0.73)	(0.03, 0.51)	(0.14, 2.32)	(0.18, 3.02)
Navier–Stokes	(0.04, 0.75)	(0.04, 0.64)	(0.15, 2.59)	(0.22, 3.60)

Table 3: Number of trainable parameters in the neural network

Dataset	Neural network size	
	Vanilla	Reduced
Darcy flow	3,420,417	101,633
Hyperelasticity	3,716,482	249,858
Navier–Stokes	3,716,482	496,770

5 Discussion

In this work, we proposed a new neural operator–Derivative-enhanced Deep Operator Network (DE-DeepONet). Compared to vanilla DeepONet, DE-DeepONet receives a reduced representation of input function and has two additional loss terms, which are for the supervised learning of the derivative of the output with respect to the inputs of both the branch net and the trunk net. Our experiments demonstrate that adding these two loss terms to the loss function greatly enhances the accuracy of both function approximations and derivative approximations, especially when the training data are limited.

We observe that when the training data are large enough, the benefits brought by adding derivative loss terms become less significant (that is, with more and more training data, we expect a relatively smaller increase in marginal accuracy and a relatively larger increase in marginal computational cost). However, in computational science and engineering, unlike other machine learning

fields such as computer vision, training data in complex and nonlinear physical system applications are often scarce due to the high costs of computational simulations. We demonstrated that the advantage of our method becomes more apparent for the more complex Navier–Stokes equations which require more iterations in the nonlinear solves than the hyperelasticity equation.

References

- [1] Robert J Adler and Jonathan E Taylor. *Random fields and geometry*. Springer Science & Business Media, 2009.
- [2] Lianghao Cao, Thomas O’Leary-Roseberry, Prashant K Jha, J Tinsley Oden, and Omar Ghattas. Residual-based error correction for neural operator accelerated infinite-dimensional bayesian inverse problems. *Journal of Computational Physics*, 486:112104, 2023.
- [3] Paul G Constantine. *Active subspaces: Emerging ideas for dimension reduction in parameter studies*. SIAM, 2015.
- [4] Roger G Ghanem and Pol D Spanos. *Stochastic finite elements: a spectral approach*. Courier Corporation, 2003.
- [5] Jinwoo Go and Peng Chen. Accelerating bayesian optimal experimental design with derivative-informed neural operators. *arXiv preprint arXiv:2312.14810*, 2023.
- [6] Somdatta Goswami, Minglang Yin, Yue Yu, and George Em Karniadakis. A physics-informed variational deepnet for predicting crack path in quasi-brittle materials. *Computer Methods in Applied Mechanics and Engineering*, 391:114587, 2022.
- [7] Zongyi Li, Nikola Kovachki, Kamyar Azizzadenesheli, Burigede Liu, Kaushik Bhattacharya, Andrew Stuart, and Anima Anandkumar. Fourier neural operator for parametric partial differential equations. *arXiv preprint arXiv:2010.08895*, 2020.
- [8] Zongyi Li, Nikola Kovachki, Kamyar Azizzadenesheli, Burigede Liu, Andrew Stuart, Kaushik Bhattacharya, and Anima Anandkumar. Multipole graph neural operator for parametric partial differential equations. *Advances in Neural Information Processing Systems*, 33:6755–6766, 2020.
- [9] Finn Lindgren, Håvard Rue, and Johan Lindström. An explicit link between gaussian fields and gaussian markov random fields: the stochastic partial differential equation approach. *Journal of the Royal Statistical Society Series B: Statistical Methodology*, 73(4):423–498, 2011.
- [10] Anders Logg, Kent-Andre Mardal, and Garth Wells. *Automated solution of differential equations by the finite element method: The FEniCS book*, volume 84. Springer Science & Business Media, 2012.
- [11] Lu Lu, Pengzhan Jin, Guofei Pang, Zhongqiang Zhang, and George Em Karniadakis. Learning nonlinear operators via deepnet based on the universal approximation theorem of operators. *Nature machine intelligence*, 3(3):218–229, 2021.
- [12] Lu Lu, Xuhui Meng, Shengze Cai, Zhiping Mao, Somdatta Goswami, Zhongqiang Zhang, and George Em Karniadakis. A comprehensive and fair comparison of two neural operators (with practical extensions) based on fair data. *Computer Methods in Applied Mechanics and Engineering*, 393:114778, 2022.

- [13] Dingcheng Luo, Thomas O’Leary-Roseberry, Peng Chen, and Omar Ghattas. Efficient pde-constrained optimization under high-dimensional uncertainty using derivative-informed neural operators. *arXiv preprint arXiv:2305.20053*, 2023.
- [14] John Tinsley Oden and Junuthula Narasimha Reddy. *An introduction to the mathematical theory of finite elements*. Courier Corporation, 2012.
- [15] Thomas O’Leary-Roseberry, Peng Chen, Umberto Villa, and Omar Ghattas. Derivative-informed neural operator: an efficient framework for high-dimensional parametric derivative learning. *Journal of Computational Physics*, 496:112555, 2024.
- [16] Thomas O’Leary-Roseberry, Umberto Villa, Peng Chen, and Omar Ghattas. Derivative-informed projected neural networks for high-dimensional parametric maps governed by pdes. *Computer Methods in Applied Mechanics and Engineering*, 388:114199, 2022.
- [17] Bogdan Raonić, Roberto Molinaro, Tobias Rohner, Siddhartha Mishra, and Emmanuel de Bezenac. Convolutional neural operators. *arXiv preprint arXiv:2302.01178*, 2023.
- [18] Umberto Villa, Noemi Petra, and Omar Ghattas. Hippylib: an extensible software framework for large-scale inverse problems governed by pdes: part i: deterministic inversion and linearized bayesian inference. *ACM Transactions on Mathematical Software (TOMS)*, 47(2):1–34, 2021.
- [19] Sifan Wang, Shyam Sankaran, Hanwen Wang, and Paris Perdikaris. An expert’s guide to training physics-informed neural networks. *arXiv preprint arXiv:2308.08468*, 2023.
- [20] Sifan Wang, Hanwen Wang, and Paris Perdikaris. Learning the solution operator of parametric partial differential equations with physics-informed deepnets. *Science advances*, 7(40):eabi8605, 2021.
- [21] Olivier Zahm, Paul G Constantine, Clémentine Prieur, and Youssef M Marzouk. Gradient-based dimension reduction of multivariate vector-valued functions. *SIAM Journal on Scientific Computing*, 42(1):A534–A558, 2020.

A Proofs

A.1 Proof of the Equivalence of Equation (6) and Equation (7)

By the definition of $\mathcal{C} = (\delta I - \gamma \Delta)^{-2}$, Equation (6) is equivalent to

$$\psi = \lambda(\delta I - \gamma \Delta)^2 \psi. \quad (20)$$

We first compute $(\delta I - \gamma \Delta)\psi$. To do this, let $p = (\delta I - \gamma \Delta)\psi$ and multiply both sides of this equation by a test function v and integrate

$$\begin{aligned} \int_{\Omega} p(x)v(x) \, dx &= \int_{\Omega} (\delta I - \gamma \Delta)\psi(x)v(x) \, dx \\ &= \delta \int_{\Omega} \psi(x)v(x) \, dx + \gamma \int_{\Omega} \langle \nabla \psi(x), \nabla v(x) \rangle \, dx, \end{aligned} \quad (21)$$

where, in the second equality, we use integration by parts and the assumption that the test function vanishes on the boundary. Then we substitute v with all of the finite element basis functions $\phi_1^{\text{in}}, \dots, \phi_{N_h^{\text{in}}}^{\text{in}}$ and collect the corresponding linear equations for the nodal values of p

$$A^{\text{in}} \mathbf{\psi} = M^{\text{in}} \mathbf{p}, \quad (22)$$

where the (i, j) -entries of A^{in} and M^{in} are given by

$$A_{ij}^{\text{in}} = \delta \langle \phi_j^{\text{in}}, \phi_i^{\text{in}} \rangle + \gamma \langle \nabla \phi_j^{\text{in}}, \nabla \phi_i^{\text{in}} \rangle, \quad M_{ij}^{\text{in}} = \langle \phi_j^{\text{in}}, \phi_i^{\text{in}} \rangle.$$

By Equation (20), function p satisfies $\psi = \lambda(\delta I - \gamma \Delta)p$. In the same manner we can see that

$$\lambda A^{\text{in}} \mathbf{p} = M^{\text{in}} \mathbf{\psi}. \quad (23)$$

Note that both matrices M^{in} and A^{in} are symmetric positive definite and thus nonsingular. Combining Equation (22) with Equation (23) yields

$$\lambda A^{\text{in}} (M^{\text{in}})^{-1} A^{\text{in}} \mathbf{\psi} = M^{\text{in}} \mathbf{\psi}, \quad (24)$$

or equivalently,

$$M^{\text{in}} (A^{\text{in}})^{-1} M^{\text{in}} (A^{\text{in}})^{-1} M^{\text{in}} \mathbf{\psi} = \lambda M^{\text{in}} \mathbf{\psi}. \quad (25)$$

A.2 Proof of the Equivalence of Equation (8) and Equation (10)

By Equation (8), for any test function $v \in V_h^{\text{in}}$, it holds that

$$\langle \mathcal{H}\psi, v \rangle = \langle \lambda \mathcal{C}^{-1} \psi, v \rangle. \quad (26)$$

In particular, for any $m \sim \nu(m)$, as we let v go through all of the finite element basis functions $\phi_i^{\text{in}} \in V_h^{\text{in}}$, we can show that

$$\begin{pmatrix} \langle d^* u(m; du(m; \psi)), \phi_1^{\text{in}} \rangle \\ \vdots \\ \langle d^* u(m; du(m; \psi)), \phi_{N_h^{\text{in}}}^{\text{in}} \rangle \end{pmatrix} = (\nabla_{\mathbf{m}} \mathbf{u})^T M^{\text{out}} (\nabla_{\mathbf{m}} \mathbf{u}) \mathbf{\psi}. \quad (27)$$

Indeed, by the definition of Gateaux derivative, we have

$$\begin{aligned}
du(m; \psi) &= \lim_{\varepsilon \rightarrow 0} \frac{u(m + \varepsilon\psi) - u(m)}{\varepsilon} \\
&= \lim_{\varepsilon \rightarrow 0} \sum_{i=1}^{N_h^{\text{out}}} \frac{\mathbf{u}_i(m + \varepsilon\psi) - \mathbf{u}_i(m)}{\varepsilon} \phi_i^{\text{out}}(x) \\
&= \lim_{\varepsilon \rightarrow 0} \sum_{i=1}^{N_h^{\text{out}}} \frac{\mathbf{u}_i(\mathbf{m}_1 + \varepsilon\psi_1, \dots, \mathbf{m}_{N_h^{\text{in}}} + \varepsilon\psi_{N_h^{\text{in}}}) - \mathbf{u}_i(\mathbf{m}_1, \dots, \mathbf{m}_{N_h^{\text{in}}})}{\varepsilon} \phi_i^{\text{out}}(x) \quad (28) \\
&= \sum_{i=1}^{N_h^{\text{out}}} \left(\frac{\partial \mathbf{u}_i}{\partial \mathbf{m}_1} \psi_1 + \dots + \frac{\partial \mathbf{u}_i}{\partial \mathbf{m}_{N_h^{\text{in}}}} \psi_{N_h^{\text{in}}} \right) \phi_i^{\text{out}}(x) \\
&= \phi^{\text{out}}(x) (\nabla_{\mathbf{m}} \mathbf{u}) \psi,
\end{aligned}$$

where $\phi^{\text{out}}(x) = (\phi_1^{\text{out}}(x), \dots, \phi_{N_h^{\text{out}}}(x))$ are the finite element basis functions of output function space V_h^{out} .

Then for any test function $v \in V_h^{\text{in}}$, it holds that

$$\begin{aligned}
\langle d^*u(m; p), v \rangle &= \langle p, du(m; v) \rangle \quad (\text{by the definition of adjoint operator}) \\
&= \langle \phi^{\text{out}}(x) (\nabla_{\mathbf{m}} \mathbf{u}) \psi, \phi^{\text{out}}(x) (\nabla_{\mathbf{m}} \mathbf{u}) \mathbf{v} \rangle \quad (\text{by Equation (28)}) \\
&= \mathbf{v}^T (\nabla_{\mathbf{m}} \mathbf{u})^T M^{\text{out}} (\nabla_{\mathbf{m}} \mathbf{u}) \psi,
\end{aligned}$$

where M^{out} is the mass matrix of output function space V_h^{out} , i.e., $M_{ij}^{\text{out}} = \langle \phi_j^{\text{out}}, \phi_i^{\text{out}} \rangle$ for $1 \leq i, j \leq N_h^{\text{out}}$. Note that if we replace v by the i -th finite element basis functions ϕ_i^{in} , then \mathbf{v} becomes the standard unit vector $e_i \in \mathbb{R}^{N_h^{\text{in}}}$ (with the i -th entry one and all others zero). Thus,

$$\langle d^*u(m; p), \phi_i^{\text{in}} \rangle = e_i^T (\nabla_{\mathbf{m}} \mathbf{u})^T M^{\text{out}} (\nabla_{\mathbf{m}} \mathbf{u}) \psi, \quad 1 \leq i \leq N_h^{\text{in}}.$$

Concatenating all the above equations yields

$$\begin{pmatrix} \langle d^*u(m; p), \phi_1^{\text{in}} \rangle \\ \vdots \\ \langle d^*u(m; p), \phi_{N_h^{\text{in}}}^{\text{in}} \rangle \end{pmatrix} = (\nabla_{\mathbf{m}} \mathbf{u})^T M^{\text{out}} (\nabla_{\mathbf{m}} \mathbf{u}) \psi.$$

Next, we prove that

$$\begin{pmatrix} \langle \lambda \mathcal{C}^{-1} \psi, \phi_1^{\text{in}} \rangle \\ \vdots \\ \langle \lambda \mathcal{C}^{-1} \psi, \phi_{N_h^{\text{in}}}^{\text{in}} \rangle \end{pmatrix} = \lambda A^{\text{in}} (M^{\text{in}})^{-1} A^{\text{in}} \psi. \quad (29)$$

Indeed, if we let $w = \lambda \mathcal{C}^{-1} \psi$, then similar to the argument in Appendix A.1, we have

$$\lambda A^{\text{in}} (M^{\text{in}})^{-1} A^{\text{in}} \psi = M^{\text{in}} w,$$

Note that

$$\langle w, \phi_i^{\text{in}} \rangle = e_i^T M^{\text{in}} w, \quad 1 \leq i \leq N_h^{\text{in}}.$$

Thus,

$$\begin{pmatrix} \langle w, \phi_1^{\text{in}} \rangle \\ \vdots \\ \langle w, \phi_{N_h^{\text{in}}}^{\text{in}} \rangle \end{pmatrix} = IM^{\text{in}}\boldsymbol{w} = \lambda A^{\text{in}}(M^{\text{in}})^{-1}A^{\text{in}}\boldsymbol{\psi}.$$

Combining (26), (27) and (29) yields

$$\mathbb{E}_{\boldsymbol{m} \sim \nu(\boldsymbol{m})}[(\nabla_{\boldsymbol{m}}\boldsymbol{u})^T M^{\text{out}}(\nabla_{\boldsymbol{m}}\boldsymbol{u})\boldsymbol{\psi}] = \lambda A^{\text{in}}(M^{\text{in}})^{-1}A^{\text{in}}\boldsymbol{\psi}.$$

B Experimental Details

B.1 Data generation

For all PDEs in this work, we use the class `dolfin.UnitSquareMesh` to create a triangular mesh of the 2D unit square with 64 cells in horizontal direction and 64 cells in vertical direction. For the Darcy flow equation and hyperelasticity equation, we set the direction of the diagonals as 'right', while for the Navier–Stokes equation, we set the direction of the diagonals as 'crossed'. See Figure 7 for a visualization of the unit square mesh with a 10 by 10 resolution.

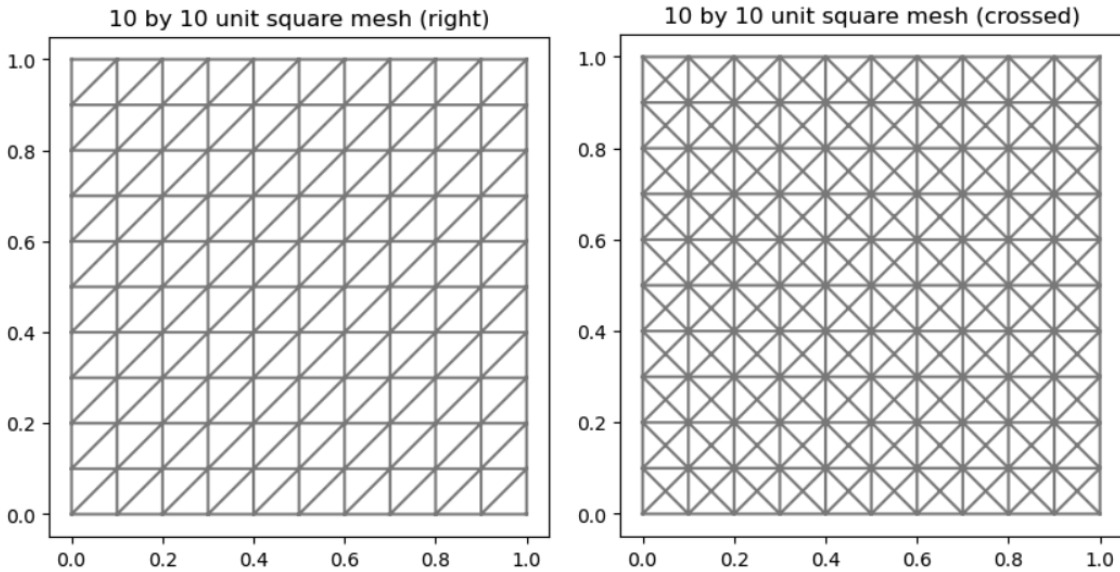


Figure 7: Visualization of the 10 by 10 unit square mesh. Left: diagonal='right'; Right: diagonal='crossed'

We use the class `dolfin.FunctionSpace` or `dolfin.VectorFunctionSpace` to create the finite element function space of input function and output function. For the finite element basis functions, we consider the Continuous Galerkin (CG) family (or the standard Lagrange family) with degree 1 or 2. See Table 4 for details.

Table 4: Configurations of data generation for different datasets

Dataset	Configurations						
	Mesh	ϕ_i^{in}	ϕ_i^{out}	$(N_{\text{train}}, N_{\text{test}})$	r	N_{grad}	s
Darcy flow	64×64 , right	CG (1D, deg=1)	CG (1D, deg=1)	(1500, 500)	16	16	10
Hyperelasticity	64×64 , right	CG (1D, deg=1)	CG (2D, deg=1)	(1500, 500)	16	16	10
Navier–Stokes	64×64 , crossed	CG (1D, deg=1)	u : CG (2D, deg=2), p : CG (1D, deg=1)	(1500, 500)	16	16	10

We generate $N_{\text{train}} = 1500$ and $N_{\text{test}} = 500$ input-output pairs $(m^{(i)}, u^{(i)})$ for training and testing, respectively. We compute first $r = 16$ KLE basis and ASM basis using double pass randomized algorithm with an oversampling parameter s of 10. In the computation of ASM basis, we use $N_{\text{grad}} = 16$ samples for the Monte Carlo estimate of the action of operator \mathcal{H} in Equation (13). In our method, we formulate the different labels into arrays with the shape as follows

- Evaluation labels: $(N_{\text{train}}, N_x, N_u)$
- Derivative m labels: $(N_{\text{train}}, N_x, r, N_u)$
- Derivative x labels: $(N_{\text{train}}, N_x, d, N_u)$

Recall that N_{train} is the number of functions used for training, N_x is the number of nodes of the mesh, N_u is the dimension of output function, r is the number of reduced basis, and d is the dimension of the domain.

B.2 Training details

For the vanilla DeepONet, we parameterize the branch net using a CNN and the trunk net using a ResNet. For the reduced basis DeepONet, both the branch net and trunk net are parameterized using ResNets. We train each model for 1000 epochs. See Table 5, Table 6 and Table 7 for details about other hyperparameters we have used. When the loss functions comprises more than two type of losses, we enhance the model’s performance and training stability by incorporating the self-adaptive learning rate annealing algorithm [19], with an update frequency of 100 and a moving average parameter of 0.9. This algorithm automatically adjusts the loss weights $\{\lambda_i\}_{i=1}^3$ in Equation (5) at a minimal computational cost. Additionally, we standardize the inputs and labels before training.

Table 5: Training details for the vanilla DeepONet

	Dataset		
	Darcy flow	Hyperelasticity	Navier–Stokes
Branch net	CNN (7 layers, 128 out dim, ReLU)	CNN (7 layers, 128 out dim, ReLU)	CNN (7 layers, 128 out dim, ReLU)
Trunk net	ResNet (7 layers, 128 out dim, ReLU)	ResNet (7 layers, 256 out dim, ReLU)	ResNet (7 layers, 256 out dim, ReLU)
Initialization	Kaiming Uniform	Kaiming Uniform	Kaiming Uniform
(lr, weight decay)	$(0.001, 10^{-6})$	$(0.001, 10^{-6})$	$(0.001, 10^{-5})$
(gamma, step size)	$(0.5, 10)$	$(0.6, 10)$	$(0.7, 10)$

Table 6: Training details for the DE-DeepONet (KLE basis + dm labels + dx labels)

	Dataset		
	Darcy	Hyperelasticity	Navier–Stokes
Branch net	ResNet (4 layers, 128 out dim, ELU)	ResNet (4 layers, 128 out dim, ELU)	ResNet (7 layers, 128 out dim, ELU)
Trunk net	ResNet (4 layers, 128 out dim, ELU)	ResNet (4 layers, 256 out dim, ELU)	ResNet (7 layers, 256 out dim, ELU)
Initialization	Kaiming Normal	Kaiming Normal	Kaiming Normal
(lr, weight decay)	(0.005, 10^{-13})	(0.001, 10^{-12})	(0.001, 0)
(gamma, step size)	(0.9, 10)	(0.99, 50)	(0.9, 20)
$N_x^{\text{batch}} (= \alpha N_x)$	633 $\approx (0.15 \times 65^2)$	422 $\approx (0.1 \times 65^2)$	422 $\approx (0.1 \times 65^2)$

Table 7: Training details for the DE-DeepONet (ASM basis + dm labels + dx labels)

	Dataset		
	Darcy	Hyperelasticity	Navier–Stokes
Branch net	ResNet (4 layers, 128 out dim, ELU)	ResNet (4 layers, 128 out dim, ELU)	ResNet (7 layers, 128 out dim, ELU)
Trunk net	ResNet (4 layers, 128 out dim, ELU)	ResNet (4 layers, 256 out dim, ELU)	ResNet (7 layers, 256 out dim, ELU)
Initialization	Kaiming Normal	Kaiming Normal	Kaiming Normal
(lr, weight decay)	(0.005, 10^{-13})	(0.001, 10^{-12})	(0.001, 10^{-12})
(gamma, step size)	(0.9, 10)	(0.99, 50)	(0.9, 10)
$N_x^{\text{batch}} (= \alpha N_x)$	633 $\approx (0.15 \times 65^2)$	422 $\approx (0.1 \times 65^2)$	422 $\approx (0.1 \times 65^2)$

B.3 Test errors

We present the comparisons of relative error on test dataset (using the metrics in Section 4.3) of different methods considered in this work in Tables 8, 9 and 10 for the Darcy flow equation, Tables 11, 12 and 13 for the hyperelasticity equation, Tables 14, 15 and 16 for the Navier–Stokes equations. For visualization, we provide the mean relative error plots in Figure 8 for the Darcy flow equation, Figure 9 for the hyperelasticity equation, and Figures 4 and 10 for the Navier–Stokes equations.

Table 8: Darcy 5 trails test relative $L^2(\Omega)$ error: mean% (standard deviation%)

Method	Number of training samples			
	16	64	256	1024
Vanilla	48.19 (5.53)	23.86 (0.77)	15.31 (0.75)	6.28 (0.33)
KLE	67.13 (4.94)	27.51 (0.95)	11.06 (0.15)	7.66 (0.09)
KLE + dm	24.40 (1.50)	10.46 (0.37)	4.89 (0.04)	4.44 (0.01)
KLE + dm + dx	22.34 (1.08)	9.39 (0.27)	4.87 (0.04)	4.47 (0.01)
ASM	63.78 (4.01)	26.26 (0.76)	10.76 (0.33)	6.87 (0.09)
ASM + dm	24.54 (1.26)	8.95 (0.18)	4.54 (0.03)	4.06 (0.02)
ASM + dm + dx	22.12 (1.03)	8.08 (0.24)	4.57 (0.02)	4.12 (0.01)

Table 9: Darcy 5 trails test relative $H^1(\Omega)$ error: mean% (standard deviation%)

Method	Number of training samples			
	16	64	256	1024
Vanilla	83.11 (3.89)	50.02 (1.93)	35.34 (1.12)	20.69 (0.36)
KLE	85.88 (7.92)	44.78 (1.22)	24.75 (0.23)	21.60 (0.12)
KLE + dm	48.27 (1.65)	27.16 (0.74)	17.44 (0.15)	15.98 (0.07)
KLE + dm + dx	39.11 (1.67)	22.57 (0.31)	16.38 (0.08)	15.41 (0.03)
ASM	82.75 (5.79)	42.62 (1.10)	24.22 (0.25)	20.43 (0.19)
ASM + dm	41.07 (1.30)	24.59 (0.33)	17.03 (0.09)	15.67 (0.08)
ASM + dm + dx	35.62 (0.45)	21.27 (0.25)	16.06 (0.07)	15.06 (0.04)

Table 10: Darcy 5 trails test relative Fro error (for dm): mean% (standard deviation%)

Method	Number of training samples			
	16	64	256	1024
Vanilla	86.27 (3.25)	61.71 (2.02)	45.89 (2.89)	25.89 (2.32)
KLE	119.02 (5.27)	65.16 (2.02)	29.90 (0.38)	23.18 (0.27)
KLE + dm	57.11 (1.82)	28.97 (1.09)	11.06 (0.20)	8.89 (0.03)
KLE + dm + dx	55.32 (1.81)	26.42 (0.85)	11.21 (0.19)	9.20 (0.04)
ASM	120.13 (6.00)	62.25 (2.26)	28.83 (0.59)	20.44 (0.14)
ASM + dm	61.02 (2.91)	24.45 (0.62)	10.68 (0.06)	8.82 (0.05)
ASM + dm + dx	56.74 (1.05)	22.59 (0.90)	10.86 (0.13)	9.20 (0.05)

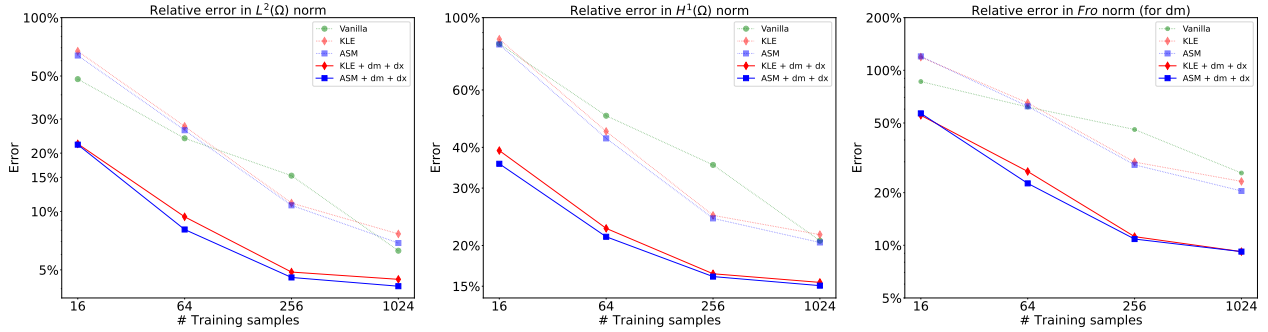


Figure 8: Mean relative errors over 5 trials with a varying number of training samples for the Darcy equation using different methods. Relative errors in the $L^2(\Omega)$ norm (left) and $H^1(\Omega)$ norm (middle) for the prediction of u . Right: Relative error in the Frobenius (Fro) norm for the prediction of $du(m; \omega_1)$.

Table 11: Hyperelasticity 5 trails test relative $L^2(\Omega)$ error: mean% (standard deviation%)

Method	Number of training samples			
	16	64	256	1024
Vanilla	45.89 (1.15)	33.28 (2.10)	17.64 (0.90)	7.82 (0.49)
KLE	80.54 (10.88)	29.29 (0.84)	12.81 (0.39)	9.14 (0.49)
KLE + dm	17.18 (1.23)	9.14 (0.76)	5.00 (0.13)	4.73 (0.34)
KLE + dm + dx	17.11 (1.50)	8.61 (0.60)	5.07 (0.21)	4.57 (0.26)
ASM	80.36 (6.16)	29.74 (3.25)	13.11 (1.15)	7.06 (0.23)
ASM + dm	21.81 (1.53)	8.71 (0.82)	4.61 (0.31)	3.47 (0.23)
ASM + dm + dx	20.24 (1.38)	8.58 (0.81)	4.90 (0.81)	3.61 (0.21)

Table 12: Hyperelasticity 5 trails test relative $H^1(\Omega)$ error: mean% (standard deviation%)

Method	Number of training samples			
	16	64	256	1024
Vanilla	57.80 (1.50)	41.87 (1.85)	26.23 (0.85)	16.77 (0.26)
KLE	80.91 (7.29)	38.88 (0.71)	21.73 (0.26)	17.46 (0.22)
KLE + dm	27.63 (0.91)	18.68 (0.17)	14.80 (0.13)	12.72 (0.27)
KLE + dm + dx	24.80 (1.01)	16.66 (0.49)	13.38 (0.31)	12.06 (0.26)
ASM	81.64 (5.59)	39.09 (1.88)	21.81 (0.50)	16.51 (0.15)
ASM + dm	31.15 (0.64)	18.76 (0.55)	14.56 (0.36)	13.02 (0.13)
ASM + dm + dx	27.38 (0.63)	16.64 (0.52)	13.26 (0.21)	11.92 (0.25)

Table 13: Hyperelasticity 5 trails test relative Fro error (for dm): mean% (standard deviation%)

Method	Number of training samples			
	16	64	256	1024
Vanilla	102.82 (0.86)	85.17 (5.59)	57.52 (3.76)	32.34 (2.33)
KLE	142.92 (11.76)	81.00 (3.57)	39.59 (0.74)	28.12 (0.83)
KLE + dm	50.93 (2.13)	25.82 (0.54)	15.39 (0.31)	13.08 (0.16)
KLE + dm + dx	43.09 (2.76)	22.16 (0.26)	12.93 (0.24)	10.91 (0.09)
ASM	138.26 (12.76)	81.01 (3.22)	37.78 (1.16)	22.47 (0.24)
ASM + dm	59.06 (1.67)	25.36 (1.41)	12.38 (0.29)	9.58 (0.05)
ASM + dm + dx	50.22 (2.48)	21.37 (0.84)	10.59 (0.12)	8.37 (0.20)

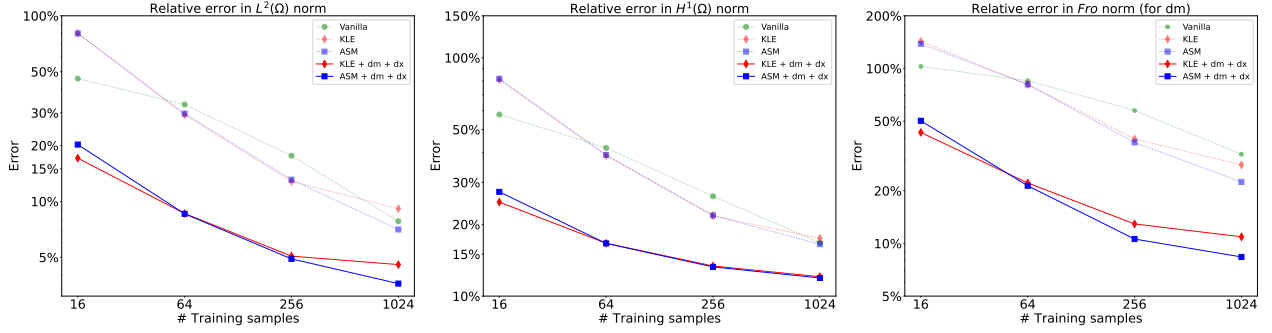


Figure 9: Mean relative errors over 5 trials with a varying number of training samples for the hyperelasticity equation using different methods. Relative errors in the $L^2(\Omega)$ norm (left) and $H^1(\Omega)$ norm (middle) for the prediction of $u = (u_1, u_2)$. Right: Relative error in the Frobenius (Fro) norm for the prediction of $du(m; \omega_1) = (du_1(m; \omega_1), du_2(m; \omega_2))$.

Table 14: Navier–Stokes 5 trails test relative $L^2(\Omega)$ error: mean% (standard deviation%)

Method	Number of training samples			
	16	64	256	1024
Vanilla	41.28 (1.17)	26.64 (1.34)	16.18 (0.86)	7.90 (0.86)
KLE	64.44 (3.01)	28.19 (1.27)	16.39 (0.09)	14.87 (0.12)
KLE + dm	24.04 (1.13)	13.84 (0.25)	11.06 (0.09)	10.44 (0.04)
KLE + dm + dx	21.89 (0.80)	13.52 (0.29)	11.06 (0.05)	10.45 (0.03)
ASM	41.61 (1.12)	18.31 (1.03)	11.16 (0.54)	9.27 (0.21)
ASM + dm	21.33 (0.62)	10.16 (0.24)	6.81 (0.05)	6.25 (0.01)
ASM + dm + dx	21.88 (0.66)	10.69 (0.25)	7.09 (0.04)	6.27 (0.01)

Table 15: Navier–Stokes 5 trails test relative $H^1(\Omega)$ error: mean% (standard deviation%)

Method	Number of training samples			
	16	64	256	1024
Vanilla	66.18 (1.42)	47.20 (2.02)	23.10 (0.80)	13.17 (0.58)
KLE	61.97 (1.44)	34.53 (1.12)	21.86 (0.19)	21.45 (0.10)
KLE + dm	51.81 (2.07)	31.57 (1.11)	18.29 (0.27)	15.40 (0.02)
KLE + dm + dx	35.54 (0.91)	27.28 (0.23)	18.53 (0.12)	15.42 (0.03)
ASM	51.19 (2.65)	28.48 (2.90)	16.48 (1.70)	14.10 (0.29)
ASM + dm	48.08 (1.27)	26.71 (0.54)	13.28 (0.37)	10.57 (0.01)
ASM + dm + dx	47.78 (2.11)	27.28 (0.41)	17.87 (0.48)	10.91 (0.17)

Table 16: Navier–Stokes 5 trails test relative *Fro* error (for dm): mean% (standard deviation%)

Method	Number of training samples			
	16	64	256	1024
Vanilla	576.93 (42.09)	375.72 (51.98)	257.51 (25.55)	212.01 (42.70)
KLE	607.06 (18.07)	293.72 (15.57)	144.20 (4.31)	165.90 (4.86)
KLE + dm	199.44 (7.48)	113.26 (7.47)	68.60 (2.01)	56.65 (0.62)
KLE + dm + dx	197.82 (10.62)	113.70 (5.85)	69.96 (2.14)	58.49 (0.39)
ASM	195.21 (9.51)	78.99 (2.44)	50.55 (0.69)	49.05 (0.60)
ASM + dm	104.05 (1.11)	52.88 (1.51)	30.67 (0.16)	26.36 (0.08)
ASM + dm + dx	102.07 (1.80)	54.23 (1.54)	31.47 (0.18)	26.03 (0.07)

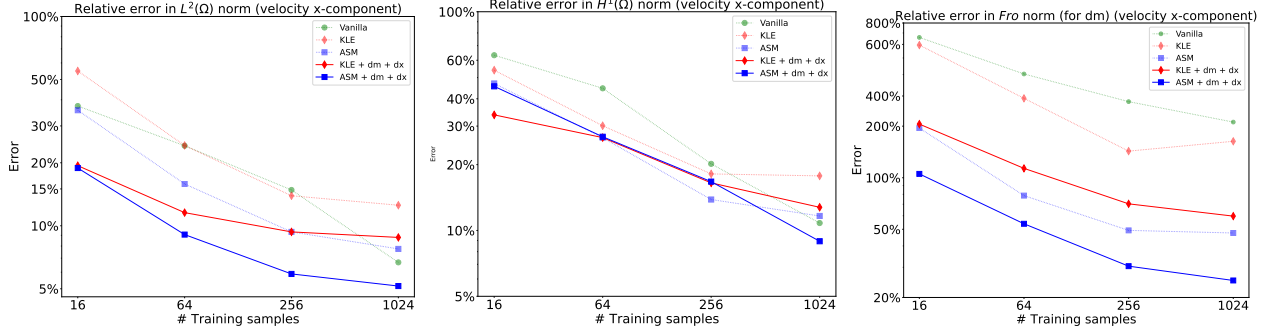


Figure 10: Mean relative errors over 5 trials with a varying number of training samples for the Navier–Stokes equations using different methods. Relative errors in the $L^2(\Omega)$ norm (left) and $H^1(\Omega)$ norm (middle) for the prediction of the velocity-x. Right: Relative error in the Frobenius (Fro) norm for the prediction of the derivative of the velocity-x with respect to the parameter in the direction of the 128 samples drawn from the same distribution as parameter.

B.4 Reduced basis

We plot the eigenvalues of KLE basis and ASM basis in Figure 11. We present visualizations of the first three KLE and ASM bases in Figure 12.

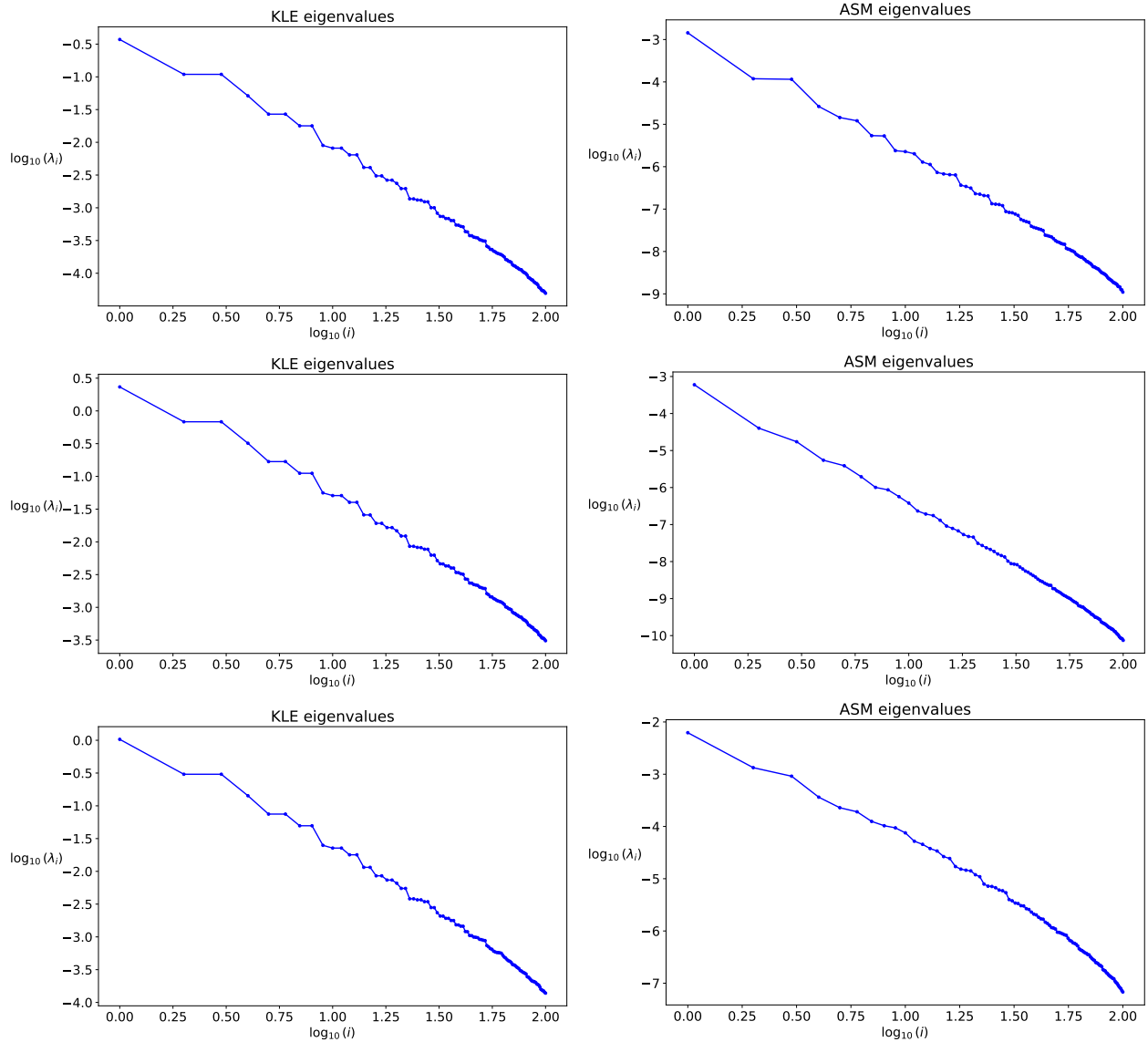


Figure 11: First 100 eigenvalues of KLE and ASM basis. Top row: Darcy; Middle row: Hyperelasticity; Bottom row: Navier–Stokes

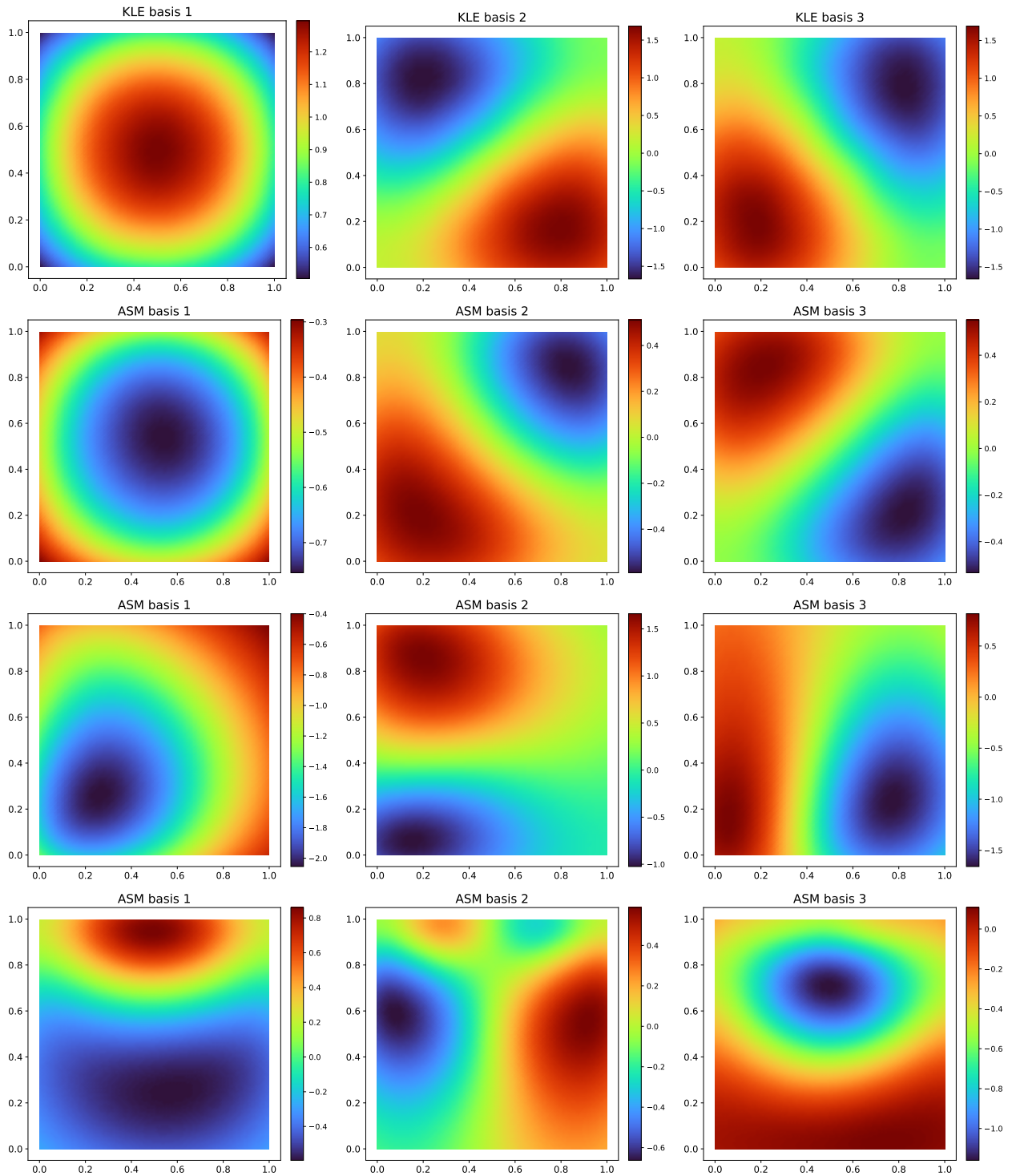


Figure 12: First row: Darcy first 3 KLE basis (similar patterns observed for Hyperelasticity and Navier–Stokes); Second row: Darcy first 3 ASM basis; Third row: Hyperelasticity first 3 ASM basis; Fourth row: Navier–Stokes first 3 ASM basis.

To measure the error induced by the projection, we define the output reconstruction error as follows

$$\frac{1}{N} \sum_{i=1}^N \frac{\|u(P_r m^{(i)}) - u(m^{(i)})\|_{L^2}}{\|u(m^{(i)})\|_{L^2}},$$

where P_r is the rank r linear projector. We provide the plots of the output reconstruction error vs number of reduced basis r using KLE basis and ASM basis in Figure 13. We can see that using the ASM basis results in a lower output reconstruction error than the KLE basis across all three equations.

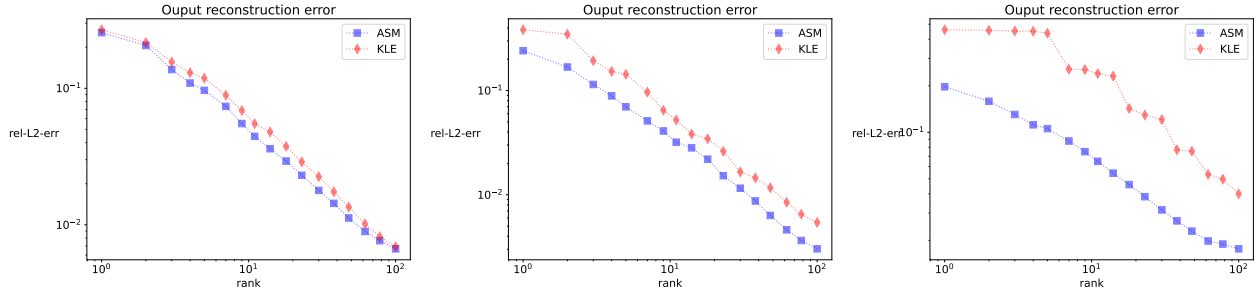


Figure 13: Output reconstruction error using KLE and ASM basis. Left: Darcy; Middle: Hyperelasticity; Right: Navier–Stokes

B.5 Visualization of the ground truth and prediction

We present the comparisons of the ground truth of solution u , model prediction \hat{u} using different methods, and absolute value of their difference $|u(x) - \hat{u}(x)|$ in Figure 14 for the Darcy flow equation, Figures 16 and 17 for the hyperelasticity equation, and Figures 5 and 20 for the Navier–Stokes equations.

We present the comparisons of the ground truth of the derivative of u with respect to m in the direction of ω_1 , denoted as $du(m; \omega_1)$, model prediction $d\hat{u}(m; \psi_1^{\text{in}})$ using different methods, and absolute value of their difference $|du(m; \omega_1) - d\hat{u}(m; \omega_1)|$ in Figure 15 for the Darcy flow equation, Figures 18 and 19 for the hyperelasticity equation, and Figures 6 and 21 for the Navier–Stokes equations.

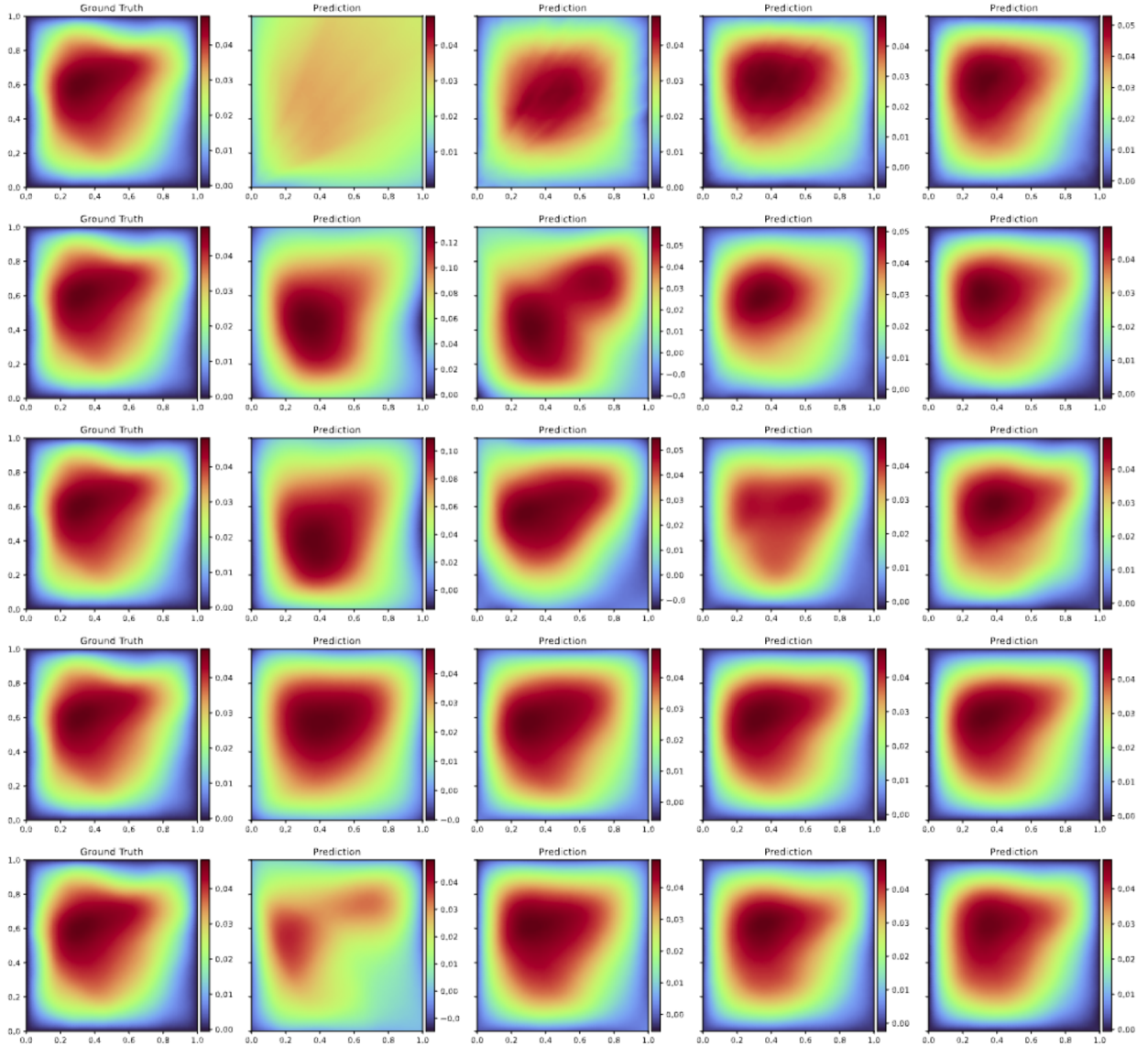


Figure 14: Darcy flow. Comparison of the predictions of u with (16, 64, 256, 1024) training samples using different methods. First row: Vanilla DeepONet; Second row: KLE; Third row: ASM; Fourth row: KLE + dm + dx; Fifth row: ASM + dm + dx.

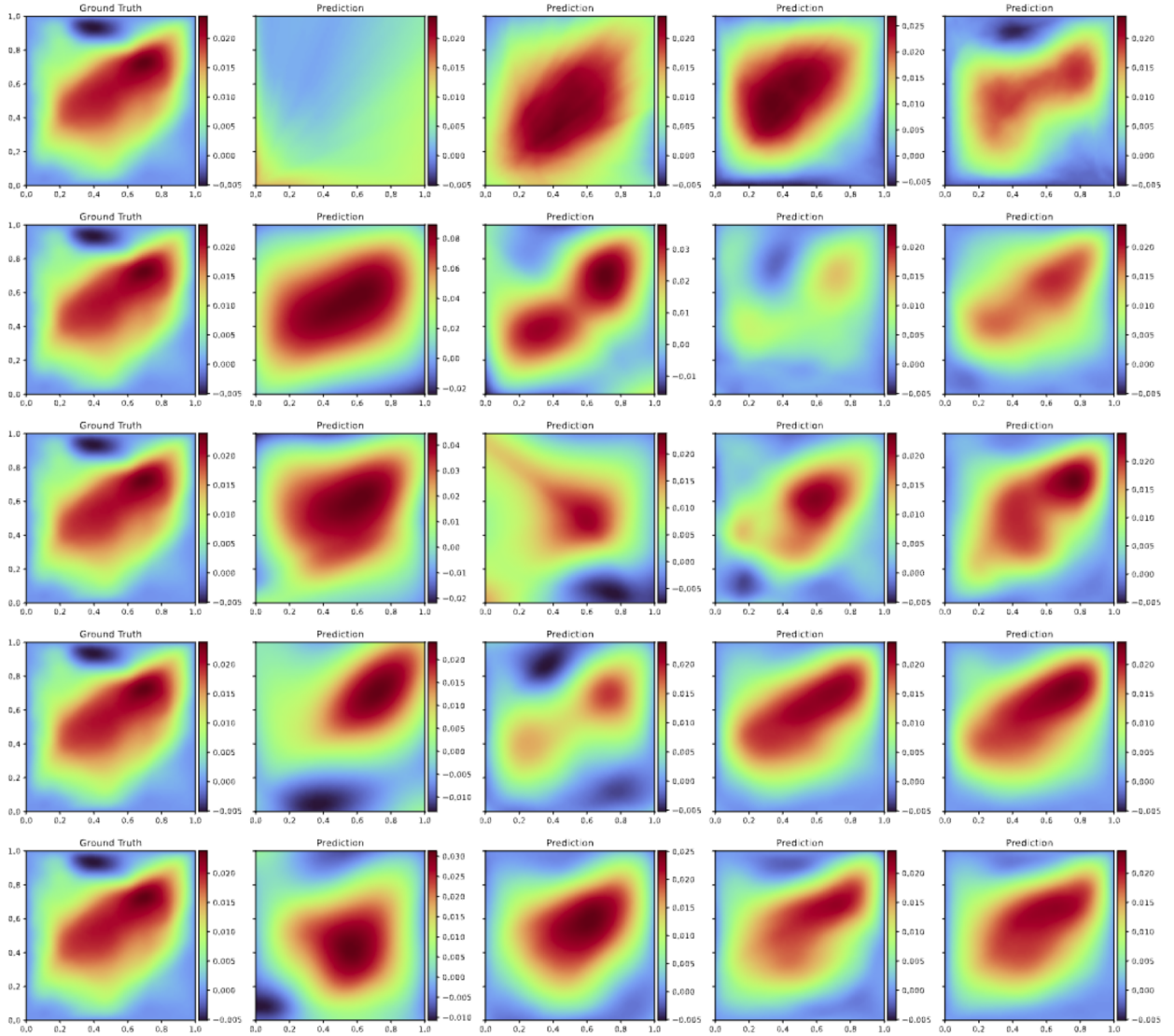


Figure 15: Darcy flow. Comparison of the predictions of directional derivative $du(m; \omega_1)$ with (16, 64, 256, 1024) training samples using different methods. First row: Vanilla DeepONet; Second row: KLE; Third row: ASM; Fourth row: KLE + dm + dx; Fifth row: ASM + dm + dx.

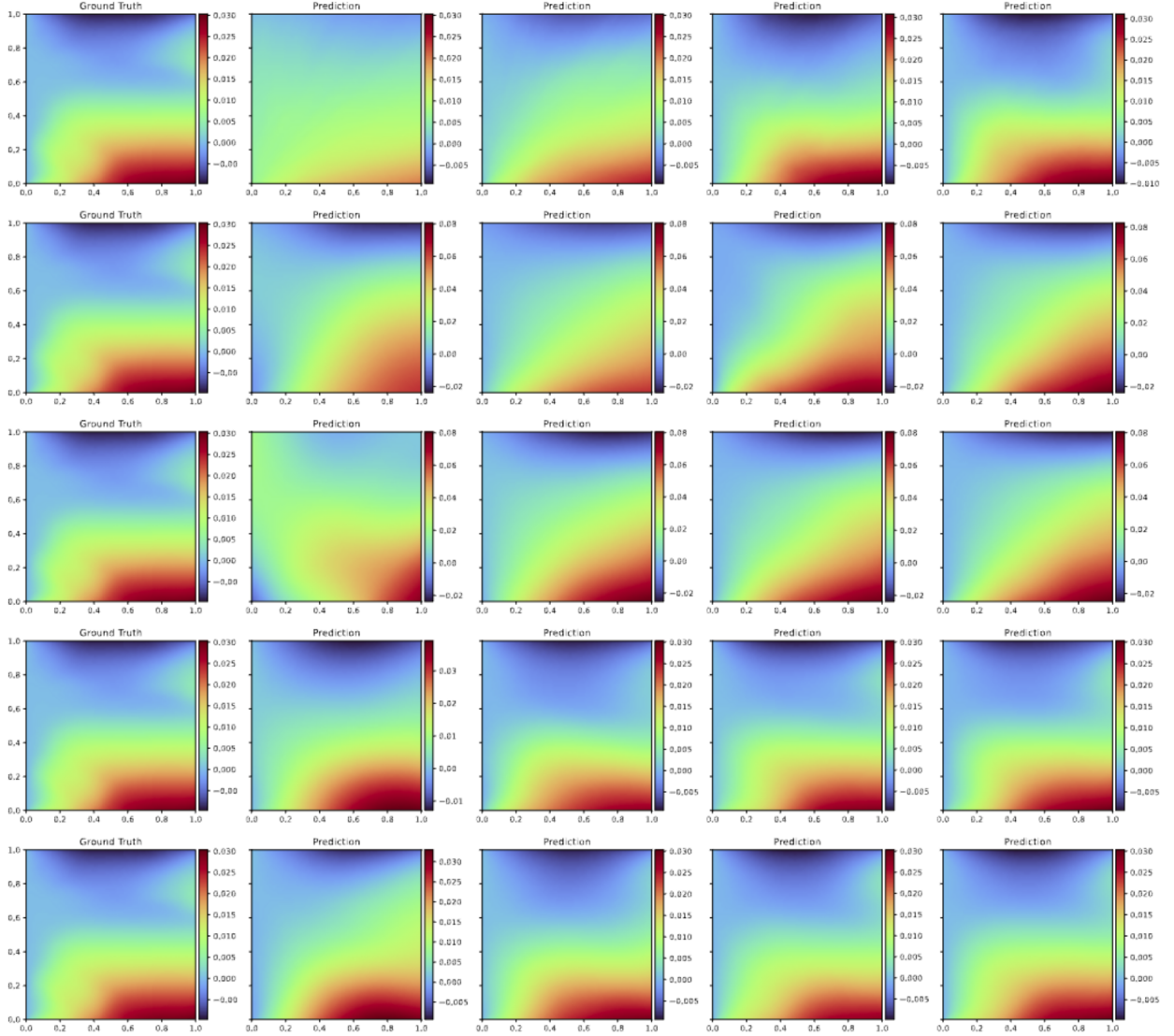


Figure 16: Hyperelasticity. Comparison of the predictions of u_1 with (16, 64, 256, 1024) training samples using different methods. First row: Vanilla DeepONet; Second row: KLE; Third row: ASM; Fourth row: KLE + dm + dx; Fifth row: ASM + dm + dx.

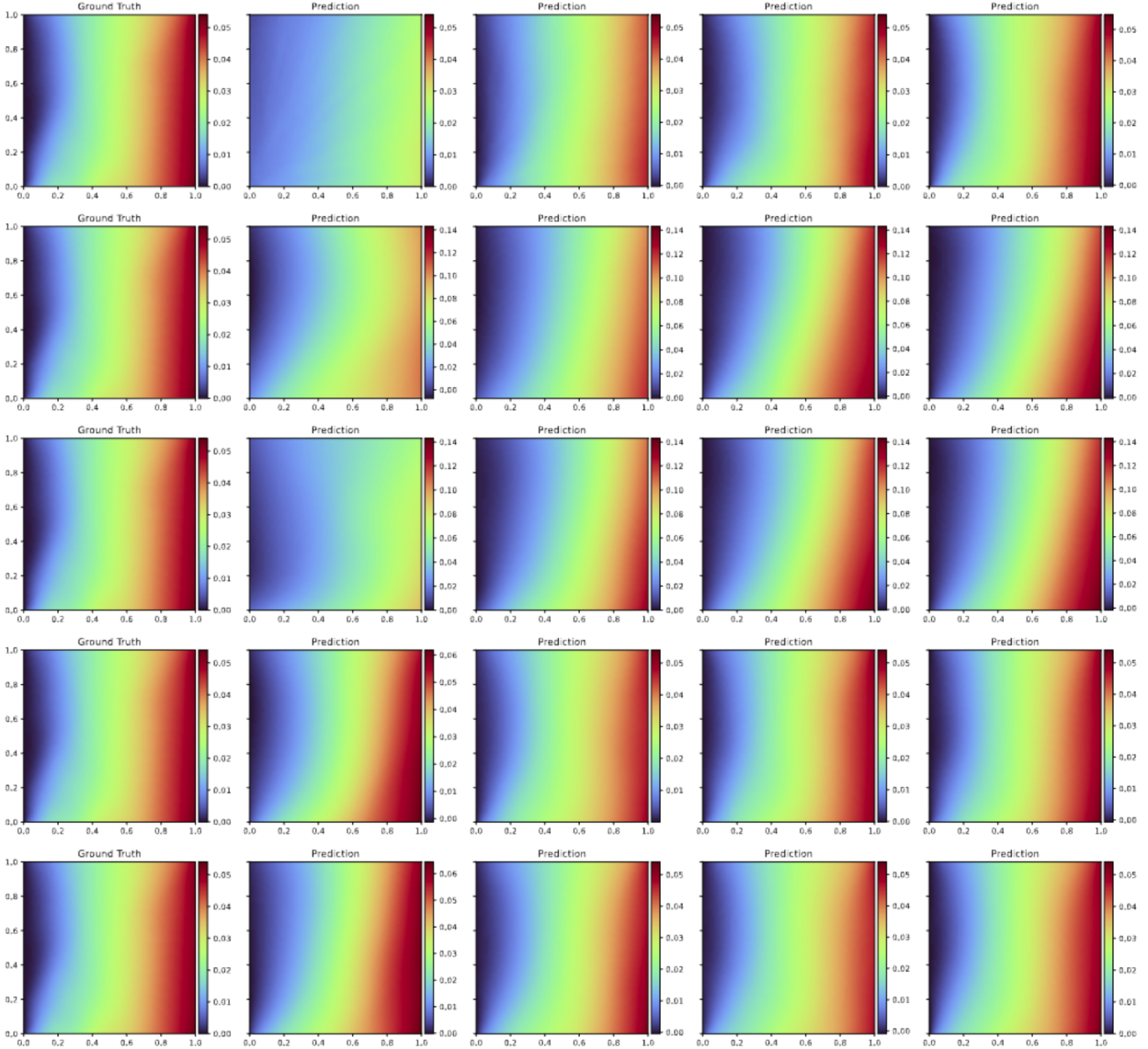


Figure 17: Hyperelasticity. Comparison of the predictions of u_2 with (16, 64, 256, 1024) training samples using different methods. First row: Vanilla DeepONet; Second row: KLE; Third row: ASM; Fourth row: KLE + dm + dx; Fifth row: ASM + dm + dx.

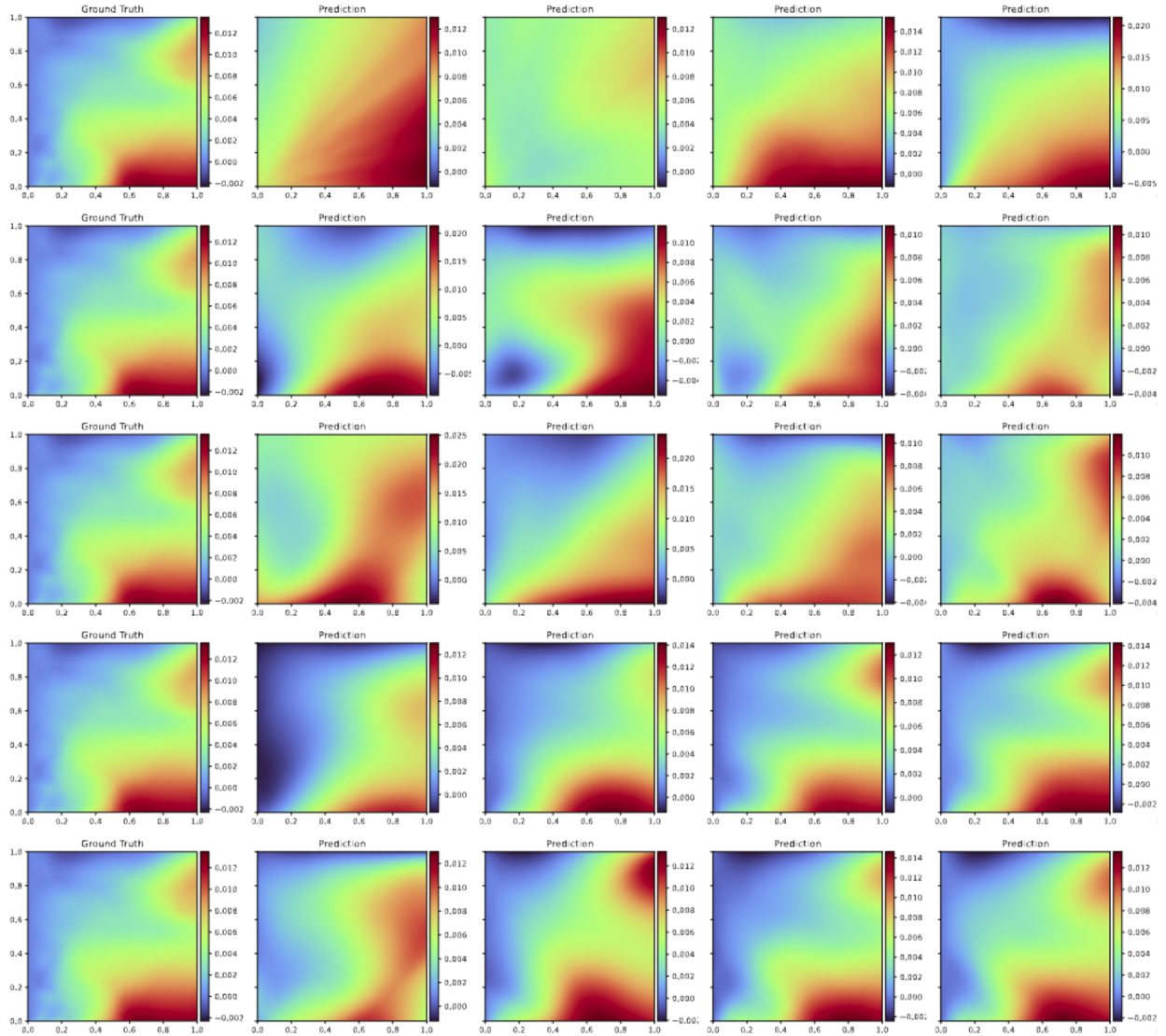


Figure 18: Hyperelasticity. Comparison of the predictions of directional derivative $du_1(m; \omega_1)$ with (16, 64, 256, 1024) training samples using different methods. First row: Vanilla DeepONet; Second row: KLE; Third row: ASM; Fourth row: KLE + dm + dx; Fifth row: ASM + dm + dx.

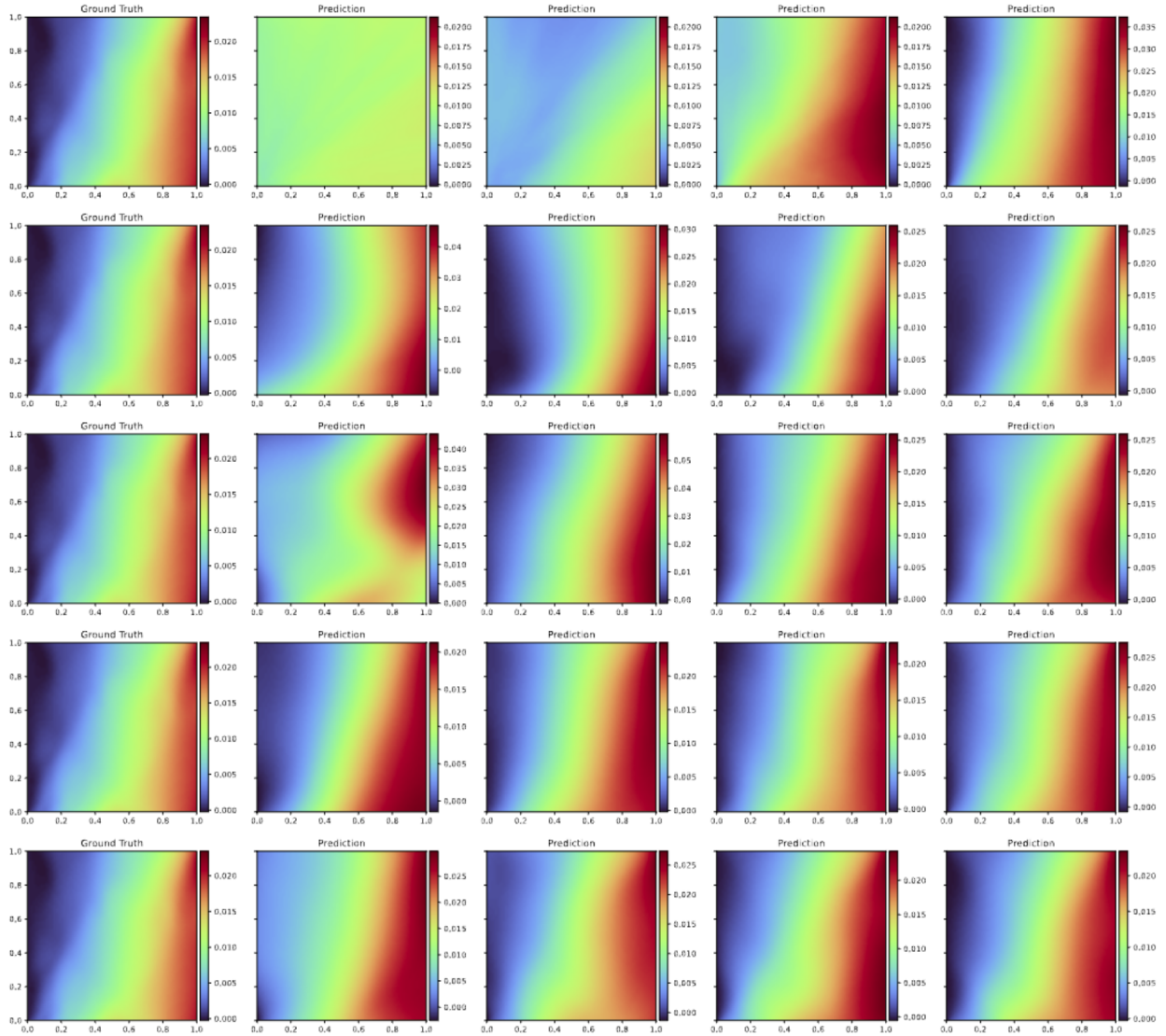


Figure 19: Hyperelasticity. Comparison of the predictions of directional derivative $du_2(m; \omega_1)$ with (16, 64, 256, 1024) training samples using different methods. First row: Vanilla DeepONet; Second row: KLE; Third row: ASM; Fourth row: KLE + dm + dx; Fifth row: ASM + dm + dx.

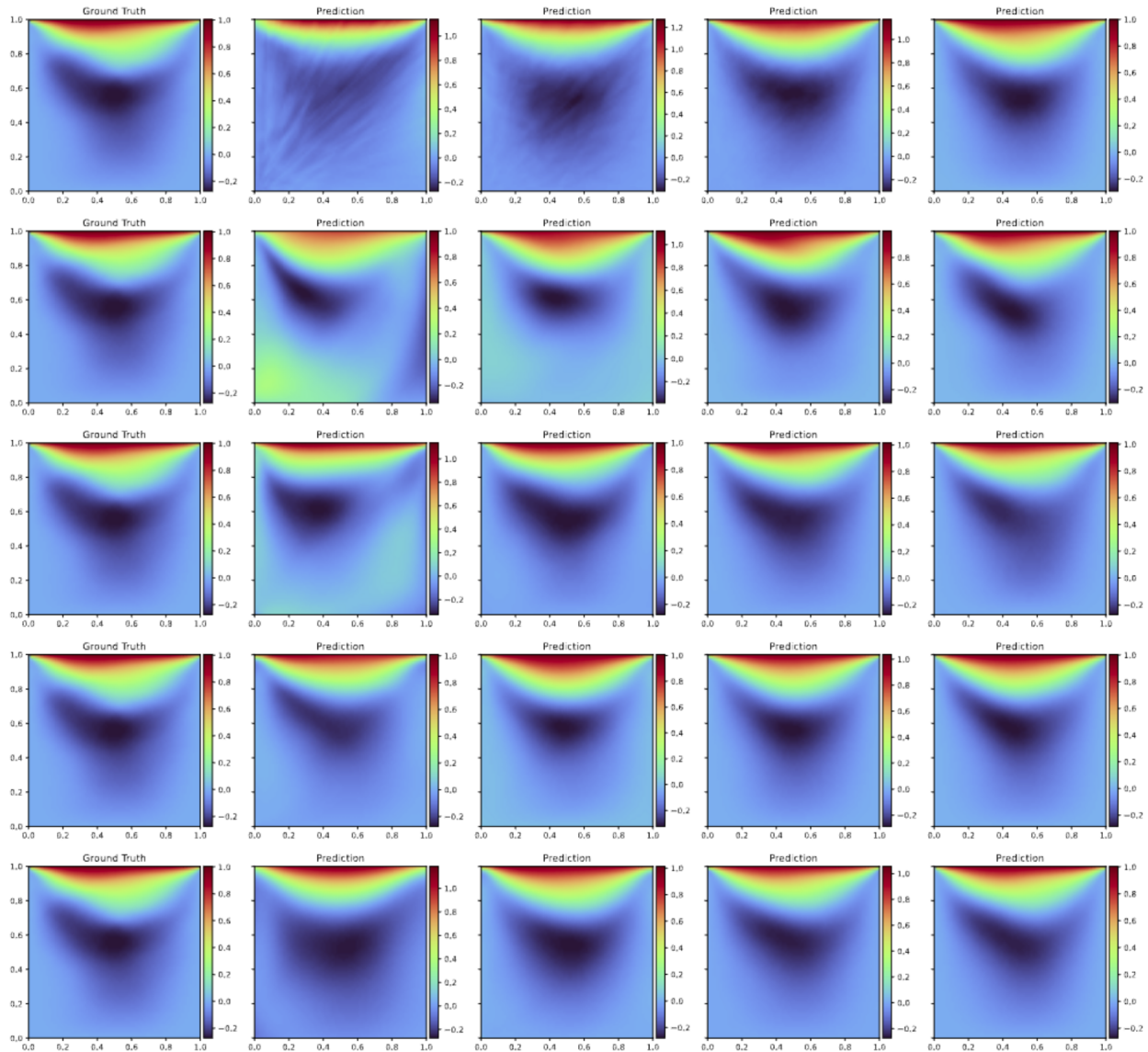


Figure 20: Navier–Stokes. Comparison of the predictions of velocity-x with (16, 64, 256, 1024) training samples using different methods. First row: Vanilla DeepONet; Second row: KLE; Third row: ASM; Fourth row: KLE + dm + dx; Fifth row: ASM + dm + dx.

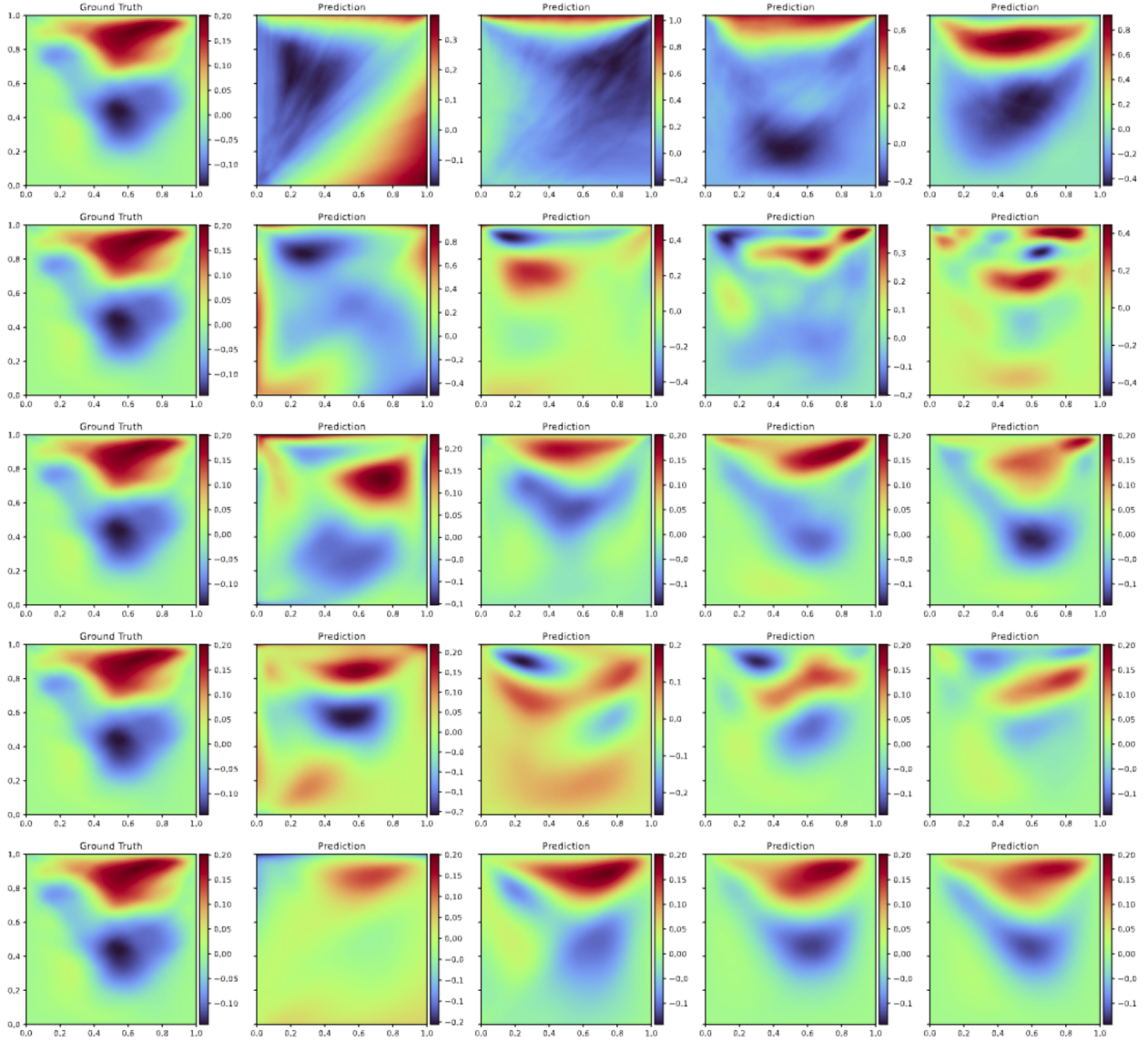


Figure 21: Navier–Stokes. Comparison of the predictions of directional derivative $du_1(m; \omega_1)$ with (16, 64, 256, 1024) training samples using different methods. First row: Vanilla DeepONet; Second row: KLE; Third row: ASM; Fourth row: KLE + dm + dx; Fifth row: ASM + dm + dx.